International Journal of Hydrogen Energy 235 (2026) 155112

Contents lists available at ScienceDirect

International Journal of Hydrogen Energy

journal homepage: www.elsevier.com/locate/he

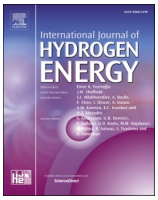

Low-temperature methanol dehydrogenation over engineered flower-like $NiMoO_4$: A pathway to clean hydrogen and anhydrous formaldehyde dual-production

Aya Farouk Farghal [a,b], Abd El-Aziz Ahmed Said [a], Mohamed Nady Goda [a,c], Shiao-Wei Kuo [b,d], Mohamed M.M. Abd El-Wahab [a,*]

[a] Department of Chemistry, Faculty of Science, Assiut University, Assiut, 71516, Egypt
[b] Department of Materials and Optoelectronic Science, Center for Functional Polymers and Supramolecular Materials, National Sun Yat-Sen University, Kaohsiung, 804, Taiwan
[c] Department of Chemistry, College of Science, Imam Mohammad Ibn Saud Islamic University (IMSIU), Riyadh, 11623, Saudi Arabia
[d] Department of Medicinal and Applied Chemistry, Kaohsiung Medical University, Kaohsiung, 807, Taiwan

ARTICLE INFO

Keywords:
H_2 evolution
Clean energy fuels
Sustainable energy source
Formaldehyde
Engineered $NiMoO_4$
Nanoflowers

ABSTRACT

Efficient and sustainable production of hydrogen (H_2) and formaldehyde (FA) is highly desirable for clean energy and chemical applications. In this work, $NiMoO_4$ nanoflowers were synthesized via a urea-assisted hydrothermal method and evaluated for non-oxidative methanol dehydrogenation. Structural and surface analyses confirmed the formation of mixed α- and β-$NiMoO_4$ phases with enhanced surface area and acidity. The optimized catalyst (N_1U_5) exhibited superior performance, achieving 100 % methanol conversion and 100 % selectivity toward H_2 and FA at 325 °C, outperforming phase-pure counterparts. The excellent catalytic behavior is attributed to the synergistic interaction between α/β phases, improved Ni–Mo redox properties, higher specific surface area, and increased surface acidity, which collectively facilitate methanol activation and charge transfer. Furthermore, the catalyst demonstrated outstanding stability for 168 h without significant deactivation. These results highlight the critical role of phase engineering and surface properties in designing highly efficient $NiMoO_4$ catalysts for selective methanol dehydrogenation.

1. Introduction

H_2 and FA are among the most strategically important compounds in both the chemical industry and the global energy landscape [1]. H_2, as a clean and sustainable energy source, has drawn more attention, especially in light of international initiatives to cut greenhouse gas emissions and switch to renewable energy sources [1,2]. H_2 is a fuel with an excellent energy density that emits only water upon combustion or during use in fuel cells [3]. It has broad applications in ammonia synthesis [4], oil refining [5,6], metal processing, and most notably in green transportation and stationary energy storage solutions [7–9]. As the wide world shifts toward a future with less emissions of carbon, the development of efficient, decentralized, and low-emission methods for H_2 generation is of paramount importance [10,11]. Despite its potential, more than 95% of the H_2 produced worldwide still originates from fossil fuels, such as coal gasification and steam methane reforming (SMR) [12–14]. These methods emit enormous amounts of carbon dioxide and undermine the environmental benefits of H_2 [12,15]. Thus, it is imperative to generate low-carbon or carbon-neutral methods for H_2 production that align with global climate goals.

Simultaneously, FA (HCHO) is one of the most widely produced organic chemicals globally. Furthermore, the global FA market was valued at approximately USD 31.69 billion in 2024 and is projected to grow at a compound annual growth rate (CAGR) of about 5% between 2025 and 2032, reaching an estimated value exceeding USD 46.82 billion by 2032 [16]. It serves as a vital precursor for manufacturing a broad spectrum of value-added products, including urea-formaldehyde and phenol-formaldehyde resins [17,18], plastics [19], textile treatments [20,21], fertilizers [22], and pharmaceutical compounds [22]. Due to its reactivity and versatility, FA continues to be indispensable in numerous industrial processes and material syntheses [23]. In addition, its wide range of applications makes FA a compound of high economic

* Corresponding author.
E-mail address: wahabm@aun.edu.eg (M.M.M. Abd El-Wahab).

https://doi.org/10.1016/j.ijhydene.2026.155112
Received 10 January 2026; Received in revised form 21 March 2026; Accepted 17 April 2026
Available online 23 April 2026

value and industrial importance [24,25]. However, traditional methods for FA synthesis-such as methanol oxidation using silver or iron-molybdenum catalysts-typically require high temperatures (250–400 °C) and involve oxygen as a co-reactant [26]. These processes are energy-intensive and can result in many unwanted byproducts, including carbon monoxide and carbon dioxide that contributing to greenhouse gas emissions; H_2O, which complicates FA purification due to the formation of hydrated FA; as well as dimethyl ether and formic acid [25–28]. Moreover, the problem of molybdenum sublimation at high temperatures leads to an extensive reduction in conversion and selectivity [25–28]. Thus, developing cleaner and more energy-efficient methods for FA production is a pressing priority. Given the importance of both H_2 and anhydrous FA, methods that allow for their simultaneous production offer a highly efficient and sustainable solution. One such promising approach is the non-oxidative methanol dehydrogenation, is a dual production and synergistic approach, in which methanol (CH_3OH) undergoes chemical transformation to produce equal amount of anhydrous FA and molecular H_2 according to Eq. (1):

$$\mathbf{CH_3OH \rightarrow HCHO + H_2} \quad (1)$$

This reaction is endothermic and requires a suitable catalyst to occur at mild conditions. Unlike oxidative processes, methanol dehydrogenation avoids the need for molecular oxygen and eliminates the risk of CO_2 formation, making it a cleaner and more energy-efficient route [29]. Furthermore, methanol is an ideal feedstock for this process because of its relatively low price, high H_2 content, and simplicity of transport and storage. Moreover, methanol can be produced from renewable sources, such as biomass or captured CO_2 combined with green H_2 [30,31], further enhancing the sustainability of this pathway. To realize this dual production pathway efficiently, the high-performance catalyst development is crucial. Where the success of methanol dehydrogenation hinges on the development of effective catalysts that can facilitate the reaction with high activity, selectivity, and stability. Numerous catalytic systems have been explored for the non-oxidative dehydrogenation of methanol to H_2 and FA, including transition-metal oxides, Na_2CO_3, β-Ga_2O_3, zeolites, and supported metal oxides such as ZnO, CuO, Ag_2O, and Au, as well as $CaMoO_4$, SO_4^{2-}–$Ce_2(MoO_4)_3/SiO_2$, and $Zr(MoO_4)_2$. For example, Ag–SiO_2–MgO catalysts reached 96 % conversion and 78 % selectivity at 650 °C [32]. In_2O_3/Na_2CO_3 catalysts achieved 60 % methanol conversion with 75 % selectivity at 677 °C [33]. While Ag–SiO_2–Al_2O_3–ZnO systems provided 99 % conversion and 87 % selectivity at 650 °C [34]. La–ZnO/SiO_2 catalysts exhibited 34 % conversion and 73 % selectivity at 600 °C [35]. Similarly, ZnO/SiO_2 and $4Ga/SiO_2$ catalysts showed 57 % conversion with 77 % selectivity and 74 % conversion with 70 % selectivity at 550 °C, respectively [36,37]. Cu/SiO_2 and β-Ga_2O_3 catalysts delivered 50 % conversion with 80 % selectivity and 65 % conversion with 70 % selectivity at 500 °C [38,39]. Furthermore, molybdates have attracted a lot of attention lately. For example: a 5 wt% MoO_3/HAP, $CaMoO_4$, SO_4^{2-}-$Ce_2(MoO_4)_3/SiO_2$ catalysts showed 100 % conversion for all and 97, 98, 100 % selectivity at 400 °C, and finally $Zr(MoO_4)_2$ with Zr:TEA ratio 1:1 (Z_1T_1) provided 99 % conversion and 95 % selectivity at 325 °C [29,40–42]. Despite these advances, most reported catalysts operate at relatively high temperatures and often provide moderate conversion and/or selectivity. In contrast, the catalyst developed in the present study achieves complete methanol conversion with 100 % H_2 and FA selectivity at a significantly lower reaction temperature (325 °C), highlighting its superior catalytic efficiency. So, among various catalysts studied, nickel molybdate ($NiMoO_4$) has become a particularly attractive material due to its outstanding properties. $NiMoO_4$ is a mixed-metal oxide known for its redox properties, thermal stability, tunable surface properties, and ability to activate O–H and C–H bonds in organic molecules [43,44]. Recent advancements in nanotechnology have enabled the synthesis of nanostructured $NiMoO_4$, such as flower-like morphologies, which offer a high surface area, abundant active sites, and enhanced electron transport [45]. These characteristics significantly improve methanol adsorption, bond activation, and product desorption, leading to more efficient and selective dehydrogenation reactions. In this context, optimizing the catalytic dehydrogenation of methanol over flower like $NiMoO_4$ not only offers a sustainable route for the large-scale production of H_2 and FA, but also contributes to the advancement of green chemistry and clean energy technologies. So, the current investigation is the synthesis of nanoflower like $NiMoO_4$ and many studies on optimizing this synthesis and its influence on its surface, acidity properties and catalytic performance. Also, we characterize these catalysts with verity of techniques like TGA, DSC, XRD, FT-IR, XPS, ICP, HR-SEM, HR-TEM, N_2 adsorption-desorption investigations, and pyridine-TPD to give all information about thermal stability, structural, textural, morphological and acidic properties of these catalysts. The investigated catalyst offered an amazing conversion and excellent selectivity to both H_2 and FA production.

2. Experimental portion

2.1. Resources

Every chemical was used exactly as it was purchased, without any purification. Nickel nitrate hexahydrate ($Ni(NO_3)_2.6H_2O$; WINLAB; 99.00%), Sodium molybdate dihydrate ($Na_2MoO_4.2H_2O$; Alpha; > 99.00%), urea ($CO(NH_2)_2$; 99.50%), Methanol (MeOH; CH_3OH, 99.60%), isopropyl alcohol (IPA, $CH_3CHOHCH_3$, 99.50%), pyridine (PY, C_5H_5N, 99.50%) and 2,6-dimethyl pyridine (DMPY, C_7H_9N, 99.90%) were all from Sigma-Aldrich.

2.2. Synthesis of $NiMoO_4$

Using hydrothermal approach and urea as a fuel, the nickel molybdate nanoflower catalysts were prepared as shown in Scheme 1. This procedure involves the dissolving of nickel nitrate hexahydrate and sodium molybdate dihydrate, with equal molar ratio (1:1), independently in an equal volume of distilled water (Total 80 mL). Utilizing magnetic stirring, the solution of sodium molybdate was dropwisely poured to the solution of nickel nitrate to create a homogenous mixture (pH = 5.70). For 60 min, the entire recipe was stirred. Afterward, the urea solution with various molar ratios (0, 1, 3, 5, 7) with respect to the ratio of nickel nitrate was prepared and poured to the previous nickel molybdate. Following then, it was moved to a 120 mL stainless-steel autoclave walled by Teflon and hydrothermally heated at 160 °C for 12 h. After the product had cooled, it was filtered well, by distilled water, and then left for drying at 70 °C For 12 h. Finally, and for 3 h, the green powder was annealed at 400–600 °C. For ease of understanding, the Ni:urea molar ratios were given as: (N_1U_y, where $y = 0, 1, 3, 5, 7$). The prepared catalysts will be simply referred to as N_1U_y, in which y represents the quantity of urea in moles. In order for assessing the best preparation conditions, a thorough investigation was conducted into the impacts of hydrothermally preparation temperatures, hydrothermal preparation periods, and heat treatment temperatures (annealing temperatures) on the highest efficient catalyst (the optimum Ni:urea molar ratios). Significant studies were conducted on the highest active Ni:urea molar ratio catalyst, which was synthesized hydrothermally for 12 h at 100, 120, 140, 160, and 180 °C. The catalyst that was hydrothermally prepared at 120 °C was done so at several times of 6, 12, 18, and 24 h to attain the optimal hydrothermal time.

3. Results and discussion portion

3.1. Catalyst characterization

To clarify the thermal changes of the precursor powder, TG and DSC curves of optimized $NiMoO_4$ precursor (N_1U_5) were done and portrayed in (Fig. S1, see Supplementary Information). After heating the precursor from ambient temperature to 800 °C, three thermal steps were observed

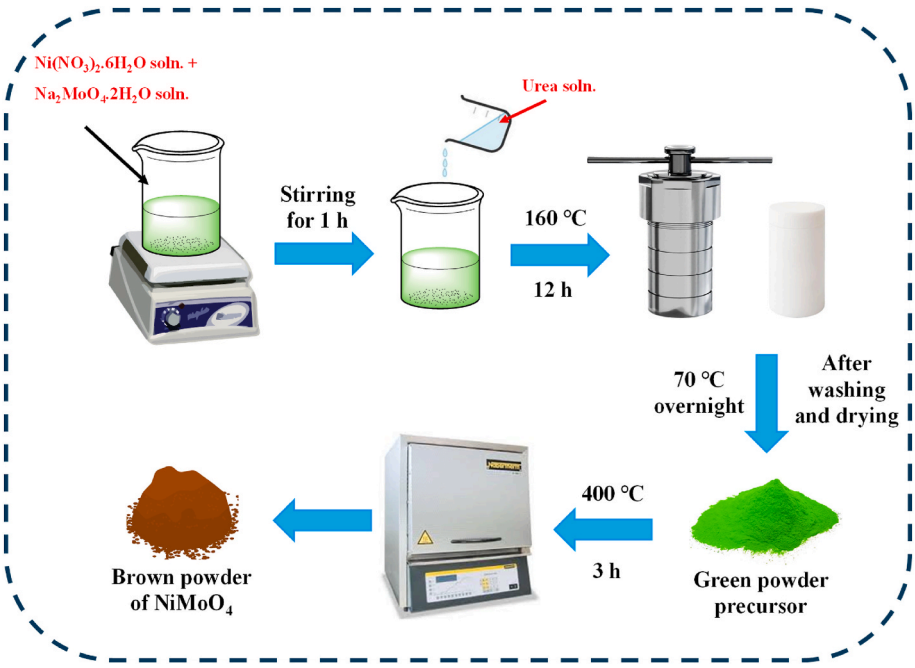

Scheme 1. Steps for $NiMoO_4$ catalyst preparation.

with 20.2 % full loss of weight. Within a temperature range of 29-150 °C, The first loss of ≈ 9.2 % is fallen and coupled with endothermic peak on DSC sintered at 102 °C, may assigned to elimination of physically adsorbed and structural water. The second and third losses (11 %) were shown in a temperature range of 150-540 °C and related to two broad exothermic peaks maximized at 310 and 580 °C, respectively. These events are assigned to the decomposition of intermediate complex formed from reaction between precursors with urea i.e., the self-propagating combustion reaction between them [46,47].

The patterns in XRD of N_1U_y catalysts (where $y = 0, 1, 3, 5, 7$), which hydrothermally heated for 12 h at 160 °C and heat-treated at 400 °C, are seen in Fig. 1a. It illustrated that the pure $NiMoO_4$ without any additives (N_1U_0) is a monoclinic of almost α-$NiMoO_4$ (major phase, JCPDS no. 33–0948) and β-$NiMoO_4$ (minor phase, JCPDS no. 45-0142). At 2θ of 14.3°, 25.3°, 28.8°, 32.6°, 43.9°, 47.4° and 53.4°, the patterns of α-$NiMoO_4$ were seen and they corresponded to (110), (−112), (220), (022), (330), (−204) and (510) respectively [45,48–50]. Whereas, β-$NiMoO_4$ is correlated with the diffraction patterns at 2θ of 18.9°, 26.6°, 38.6° and 41.18° which are correspond to (101), (220), (−132) and (040), respectively [48,51]. As the ratios of urea ($y = 0, 1, 3, 5, 7$) rise, the formation of β-$NiMoO_4$ increases, where at 2θ of 34° corresponds to (22-2) plane [52,53], another peak that is ascribed to β-$NiMoO_4$ is seen, and the crystallinity decreases (Fig. 1a). Moreover, Fig. 1b depicted the hydrothermal preparation temperatures influence on the crystal structure of $NiMoO_4$ (N_1U_5) catalyst for 12 h. It shows that all samples are semicrystalline with increasing the peak intensity at 2θ of 34° which linked to β-$NiMoO_4$, as rising in the hydrothermal preparation temperature. Fig. 1c demonstrated the annealing temperature influence on the crystallinity and crystal structure of N_1U_5 catalyst hydrothermally heated at 120 °C for 12 h; where the sample annealed at 400 °C is semicrystalline with combination of two phases of α and β-$NiMoO_4$. However, as the annealing temperature rises, the crystallinity and the β-phase formation increase. The broad and low-intensity of XRD patterns illustrated that the smaller size of prepared $NiMoO_4$ are nanocrystalline in nature [46,52]; as demonstrated by the computed particle sizes (D_{BET}) using S_{BET}, SEM, and TEM pictures in the subsequent sections.

To confirm the presence of $NiMoO_4$, the FT-IR spectral analysis of $NiMoO_4$ catalysts with different Ni:urea molar ratios (N_1U_y), hydrothermal preparation temperatures and annealed at 400-600 °C are seen in Fig. 1d-f. All catalysts displayed the same spectral portions at around 3427, 1638, 963, 933, 880, 632 and 412 cm^{-1}. The broad band at 3427 cm^{-1} and the small intensity band at 1638 cm^{-1} are assigned to the adsorbed water molecules' O–H stretching and bending vibrations [54]. The characteristic vibration of $NiMoO_4$ is displayed below 1000 cm^{-1}. The MoO_4 tetrahedral found in $NiMoO_4$ is responsible for the peaks at 963 and 933 cm^{-1} [48,54,55]. In the $NiMoO_4$ lattice structure, the band at 880 cm^{-1} is attributed to Mo's tetrahedral position (structural feature of the β-phase) [56]. The signal at 632 cm^{-1} is ascribed to the Mo–O–Ni vibrations (edge-shared MoO_6 octahedra) for α-$NiMoO_4$ [53,56,57]. The crystalline $NiMoO_4$ NPs exhibit a salient small intensity band saw at 412 cm^{-1} due to the overlapping of MoO_6 and NiO_6 groups (Ni–O and Mo–O bonding vibration) [48,57,58], and this band is appeared clearly in high magnification for FT-IR spectra at 400-500 cm^{-1} as illustrated in Fig. S2.

To elucidate the morphology, surface topography, and elemental mapping of N_1U_5 catalyst that was synthesized at 120 °C for 12 h and followed by annealing at 400 °C, field emission scanning electron microscopy (FE-SEM) and energy-dispersive X-ray spectroscopy (EDS) mapping analyses were performed and presented in Fig. 2. The low-magnification FE-SEM image (Fig. 2a) reveals a well-defined, fully blossomed flower-like morphology composed of interconnected petal-like nanosheets. Such hierarchical nanosheet architecture provides a high surface area and abundant exposed Ni^{2+} active sites, facilitating methanol adsorption and activation. Moreover, the porous structure improves mass transport and accelerates the desorption of FA and H_2, thereby suppressing secondary oxidation reactions. The intimate contact between Ni and Mo centers within the flower-like framework promotes efficient electron transfer and redox synergy, thereby facilitating more efficient catalytic activity and selectivity [59,60]. Higher-magnification FE-SEM images (Fig. 2b and c) further highlight the intricate nanosheet arrangement and structural uniformity of the nanoflowers. Elemental mapping of the $NiMoO_4$ nanoflowers (Fig. 2d–i) confirms the homogeneous spreading of nickel, molybdenum, oxygen, carbon, and nitrogen throughout the catalyst, validating the successful formation of the $NiMoO_4$ nanoflower framework.

On the other side, the TEM pictures of the optimized N_1U_5 catalyst, that was synthesized at 120 °C for 12 h and followed by annealing at

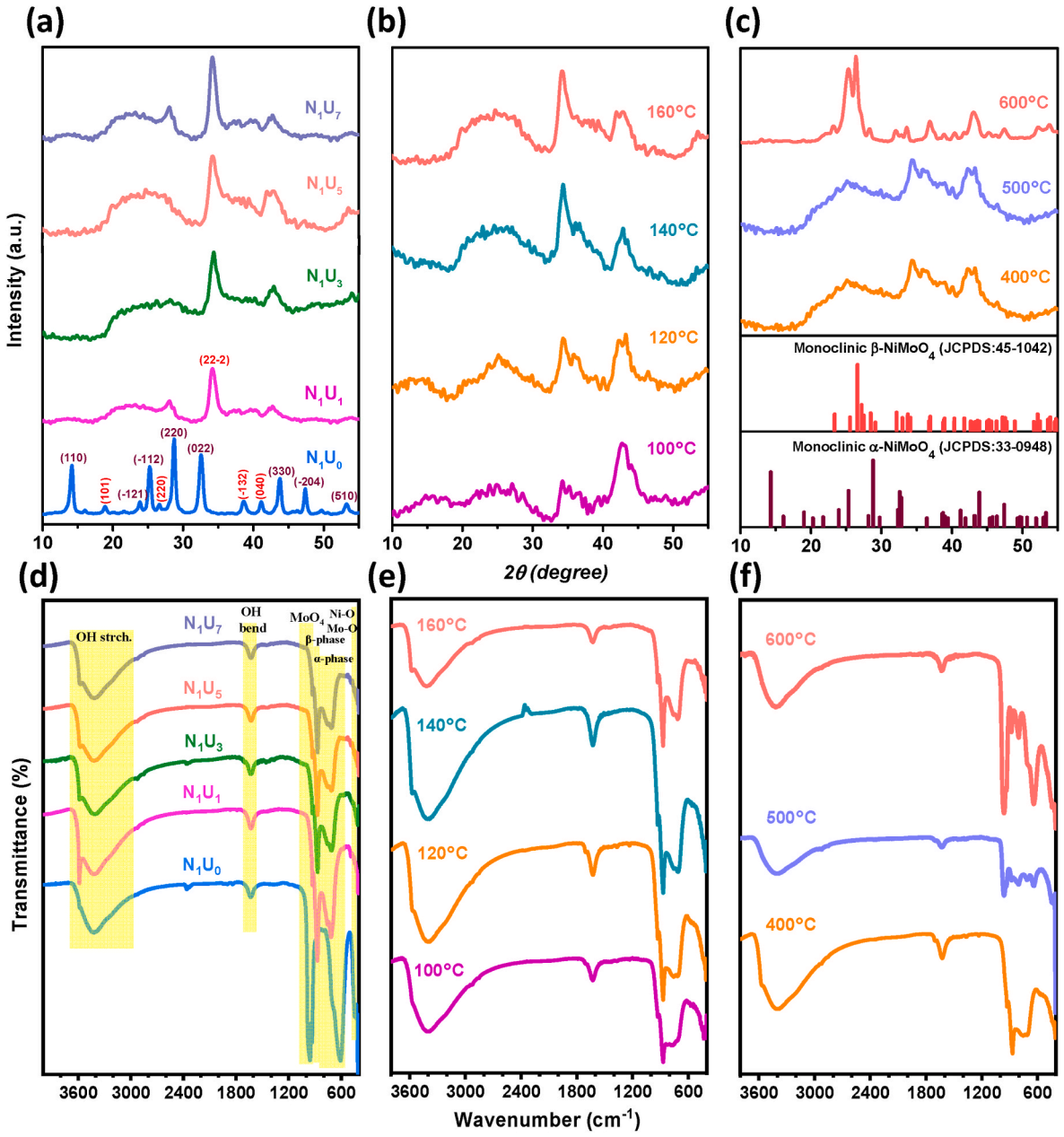

Fig. 1. XRD profiles and FT-IR spectra of (a,d) influence of urea molar ratios (N_1U_y) for catalyst series, (b,e) influence of hydrothermal temperature, (c,f) influence of annealing temperatures.

400 °C, are portrayed in Fig. 3. The low-magnification TEM picture (Fig. 3a, scale bar: 200 nm) reveals that the ultrathin nanosheets are interconnected, forming a highly open and porous three-dimensional network, consistent with the flower-like morphology observed in the SEM analysis [45,61]. Such hierarchically porous nanosheet architecture enhances surface area and mass transport pathways, thereby contributing to the catalytic activity of the $NiMoO_4$ nanostructure. High-resolution TEM pictures (Fig. 3b–d further display well-defined lattice fringes and crumpled silk-like structure features characteristic of $NiMoO_4$ nanosheets [45,61,62]. The corresponding TEM-EDS spectrum (Fig. 3e) confirms the exitance of nickel, molybdenum, oxygen, carbon, and nitrogen, in agreement with the SEM-EDS results, validating the successful formation of $NiMoO_4$ nanoflower catalyst.

After having a proper understanding of the structural and morphological features of $NiMoO_4$ catalyst (N_1U_5), its surface elemental chemical composition and oxidation states were examined by X-ray photoelectron spectroscopy (XPS). The overview XPS spectrum (Fig. 4a) observes characteristic signals for the elements: nickel, molybdenum, oxygen, carbon and nitrogen in $NiMoO_4$ (N_1U_5). The Ni 2p XPS spectrum of nickel molybdate (Fig. 4b) presents two well-defined peaks at binding energies of 857.74 and 875.38 eV, ascribed to the Ni $2p_{3/2}$ and Ni $2p_{1/2}$ core levels, respectively, and a spin–orbit splitting separation of about 17.6 eV. In addition to these main features, pronounced shake-up satellite peaks appeared at 863.11 and 881.37 eV. Such spectral characteristics are indicative of Ni^{2+} species [63–66]. The Ni $2p_{3/2}$ main peak was deconvoluted into two components located at 855.7 and 857.7 eV, which are attributed to Ni^{2+} species in slightly different chemical environments within the $NiMoO_4$ structure (α and β) [67,68]. In Ni-based oxides, the Ni $2p_{3/2}$ region typically exhibits peak broadening and asymmetry due to variations in the local Ni–O coordination, surface hydroxylation, and multiplet splitting effects associated with Ni^{2+} species [63–66,69]. Meanwhile, Mo 3d XPS spectra (Fig. 4c) observes two prominent peaks at binding energies of 232.71 and 235.81 eV, which are related to Mo $3d_{5/2}$ and Mo $3d_{3/2}$, respectively, which belongs to Mo^{6+}

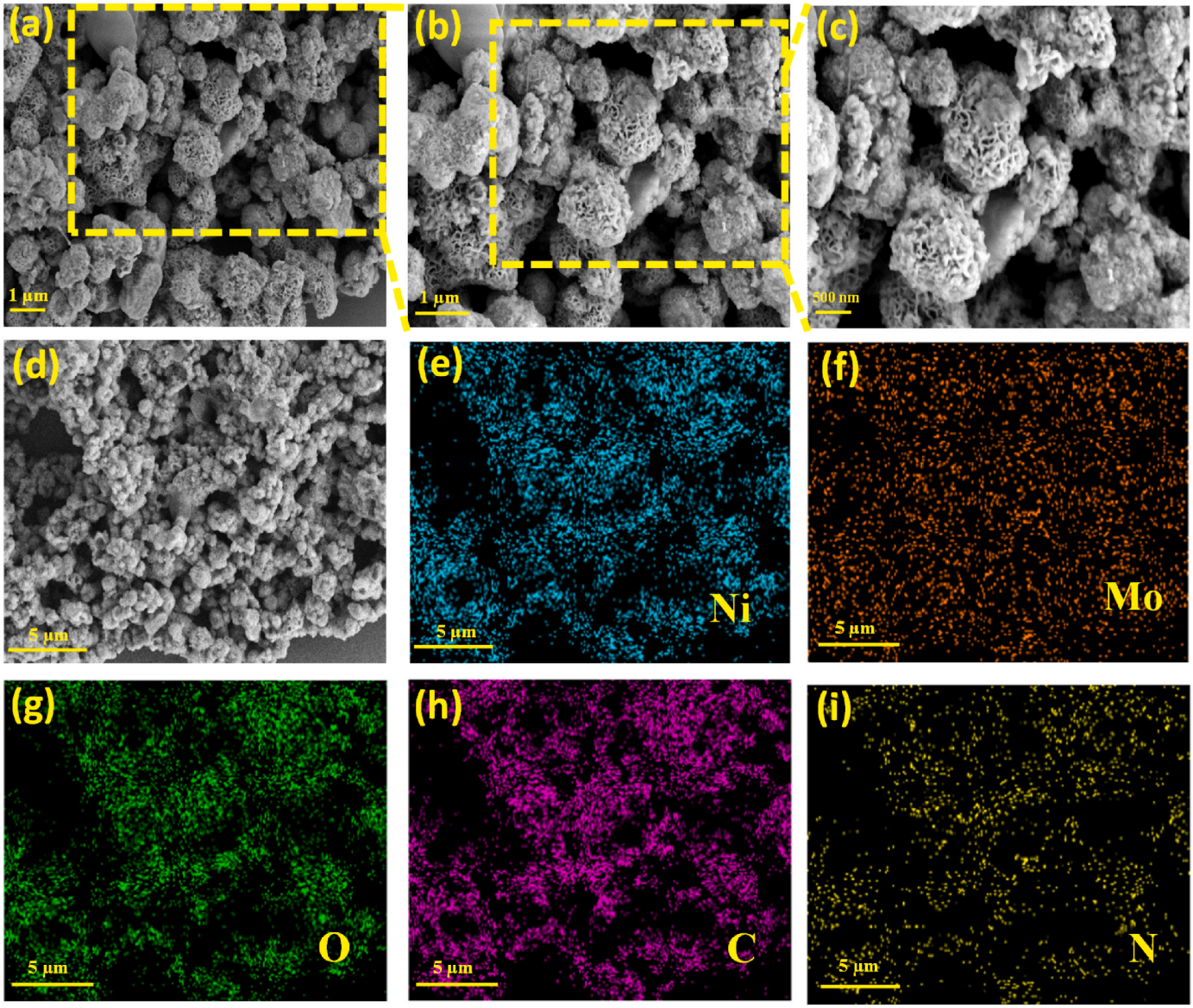

Fig. 2. FE-SEM images of (a) and (b,c) the high-resolution SEM for the yellow rectangular shapes in Fig. 2(a and b), respectively, SEM-EDS elemental mapping images (e-i) for Fig. 2(d) of the optimized N_1U_5 catalyst. (For interpretation of the references to colour in this figure legend, the reader is referred to the Web version of this article.)

[58,64,65,70,71]. Additional peaks at 230.01 and 234.51 eV correspond to Mo^{5+} species, arising from the partial reduction of Mo^{6+}. These electron-rich Mo^{5+} sites exhibit enhanced nucleophilicity, which is beneficial for promoting the dehydrogenation process [71]. In Fig. 4d, the O 1s spectra exhibits two obvious peaks that are assigned to different oxygen species. The peak at 530.3 eV is related to metal-oxygen bonding (Ni/Mo–O) and the peak at 532.9 eV matching with surface hydroxyl groups or adsorbed water molecules [58,66,72,73]. Furthermore, the spectrum of C 1s (Fig. 4e) can be separated into three distinct sections at 284.61, 286.91, and 290.02 eV, assigned to C═C/C–C, C═O, and O–C═O functionalities, respectively [47,52,54,58]. The N 1s spectrum (Fig. 4f) portrays peaks at 398.2 and 400.7 eV, attributed to –NH– (amine) and = N– (imine) species, respectively [58,70]. The existence of carbon and nitrogen-containing species is likely derived from residual urea decomposition during the calcination step. Collectively, these XPS results corroborate the successful formation of $NiMoO_4$, consistent with XRD and FT-IR analyses presented in Fig. 1.

The elemental composition of the synthesized catalysts was further examined by inductively coupled plasma (ICP) analysis to verify the Ni/Mo atomic ratio. The theoretical stoichiometry of $NiMoO_4$ corresponds to a Ni:Mo ratio of 1:1. The ICP results confirm that the experimental Ni/Mo ratios are close to the expected value (Table 1), indicating successful formation of the target $NiMoO_4$ composition and good control over the synthesis process. The slight deviations observed, if any, fall within the acceptable experimental error range and do not significantly affect the structural integrity or catalytic performance of the material. These results are consistent with the XRD and XPS analyses, further validating the phase purity and compositional reliability of the prepared catalysts.

The texture features of the prepared $NiMoO_4$ catalysts were assessed using N_2 adsorption-desorption analysis at 77 K, with the corresponding isotherms, pore size distributions and $V_{a\text{-}t}$ plots are shown in Fig. 5 and Fig. S3, and the quantitative textural parameters derived from these measurements are summarized in Table 2. All samples display type IV adsorption isotherms with a slight contribution of type II of Brunauer's classification (Fig. 5a–c), which are characterized by mesoporous nature [74]. The accompanying hysteresis loops are primarily of type H2 with a minor H3 component [75], reflecting the coexistence of ink-bottle and slit-like pores. The specific surface area (S_{BET}) of the catalysts was

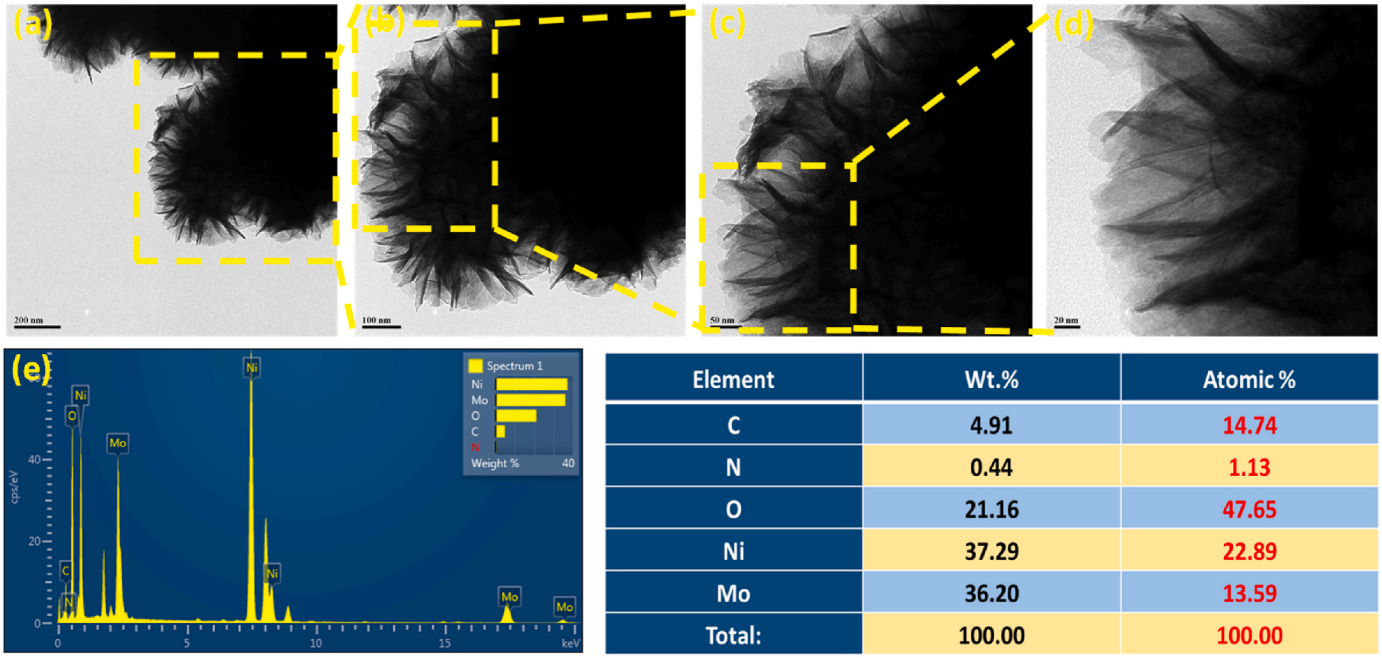

Element	Wt.%	Atomic %
C	4.91	14.74
N	0.44	1.13
O	21.16	47.65
Ni	37.29	22.89
Mo	36.20	13.59
Total:	100.00	100.00

Fig. 3. (a) TEM pictures of the optimized N_1U_5 catalyst, and (b-d) the high-resolution TEM for the yellow rectangular shapes in Fig. 3(a–c), respectively, (e) EDS mapping for N_1U_5 catalyst with its corresponding table. (For interpretation of the references to colour in this figure legend, the reader is referred to the Web version of this article.)

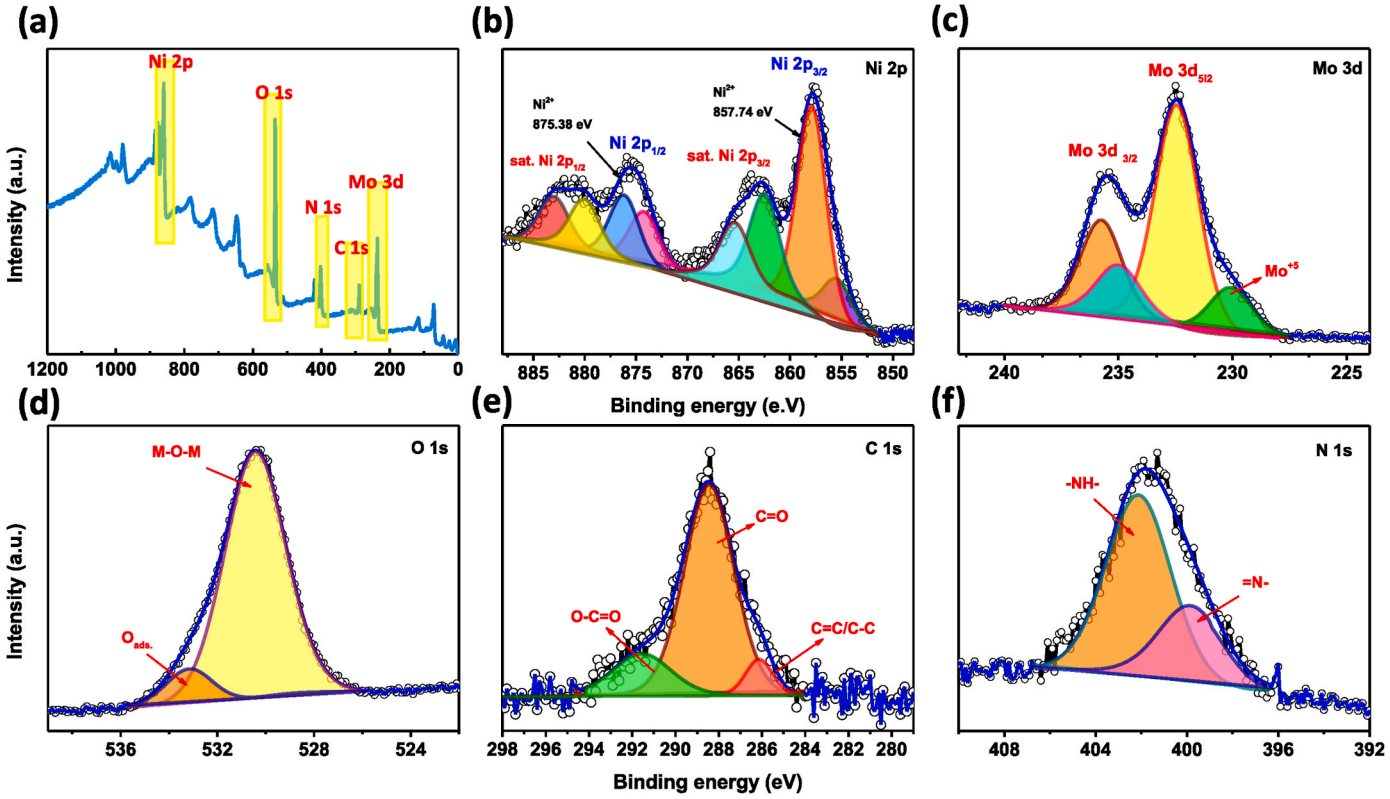

Fig. 4. (a) Overview XPS spectrum of the optimized N_1U_5 catalyst. Detailed core-level spectra for (b) Ni 2p, (c) Mo 3d, (d) O 1s, (e) C 1s, and (f) N 1s are shown.

determined using the Brunauer–Emmett–Teller (BET) equation within the conventional relative pressure range ($P/P^o = 0.05–0.30$), assuming a nitrogen molecular cross-sectional area of 16.2 Å^2. The calculated S_{BET} values are summarized in Table 2. As observed, the catalyst synthesized without urea (N_1U_0) exhibited the lowest surface area of 20.9 m^2 g^{-1}. Increasing the urea molar ratio (*y*-value) resulted in a gradual enhancement of S_{BET}, reaching a maximum value of 130.3 m^2 g^{-1} at $y = 5$. These observations demonstrate that a urea molar ratio of 5 optimizes pore development with the highest S_{BET}. However, further increases in the urea content led to a decline in S_{BET}. The impact of hydrothermal

Table 1
ICP analysis of N_1U_y catalysts.

Sample	Ni (wt.%)	Mo (wt. %)	Ni/Mo (Atomic ratio)
N_1U_0	25.79	42.33	0.996056
N_1U_1	25.72	42.25	0.995234
N_1U_3	25.58	42.22	0.994441
N_1U_5	25.45	41.81	0.999916
N_1U_7	25.10	41.05	0.999635

preparation temperature (100–160 °C) on the N_1U_5 catalyst was also evaluated. When the hydrothermal temperature is raised from 100 to 120 °C, the surface area increases from 139.8 to 154.4 $m^2\ g^{-1}$, while a further increase to 160 °C reduces it to 130.3 $m^2\ g^{-1}$. Accordingly, 120 °C is identified as the most favorable hydrothermal temperature for generating higher surface area. Elevating the annealing temperature to 600 °C results in a marked decrease in S_{BET}, primarily due to sintering and the associated enlargement of particle size [41,42,76]. The particle size (D_{BET}) was estimated from the S_{BET} and the density, and the calculated values are also portrayed in Table 2 [77,78]. As expected, D_{BET} exhibits an inverse relationship with S_{BET}. The pure $NiMoO_4$ sample (N_1U_0) displayed the largest particle size (73.6 nm) and the lowest surface area (20.9 $m^2\ g^{-1}$). With increasing urea content, the particle size decreased, reaching a minimum at $y = 5$, followed by an increase at higher urea ratios. A similar trend is observed with hydrothermal temperature: D_{BET} decreases from 11.9 nm at 100 °C to 10.0 nm at 120 °C, then increases to 12.5 nm with further increasing the temperature to 160 °C due to the reduction in S_{BET}. The total pore volume values closely parallel to the changes in S_{BET}, whereas the average pore diameter displays a less regular dependence (Table 2). Surface areas obtained using the *t*-method (S_t) closely match the BET values, confirming the suitability of the de Boer *t*-plot approach for these materials. The BJH pore size distribution curves (Fig. 5d–f) illustrates that most samples exhibit pore size maxima through the mesoporous region (2–50 nm), whereas pure $NiMoO_4$ (N_1U_0) which was annealing at 400 °C and N_1U_5 that was annealing at 600 °C show peaks below 2 nm, reflecting their microporous nature. This is consistent with the average pore diameter values in Table 2, where only these two samples have mean pore sizes below 2 nm. Moreover, The V_{a-t} plots (Fig. S3) corroborate

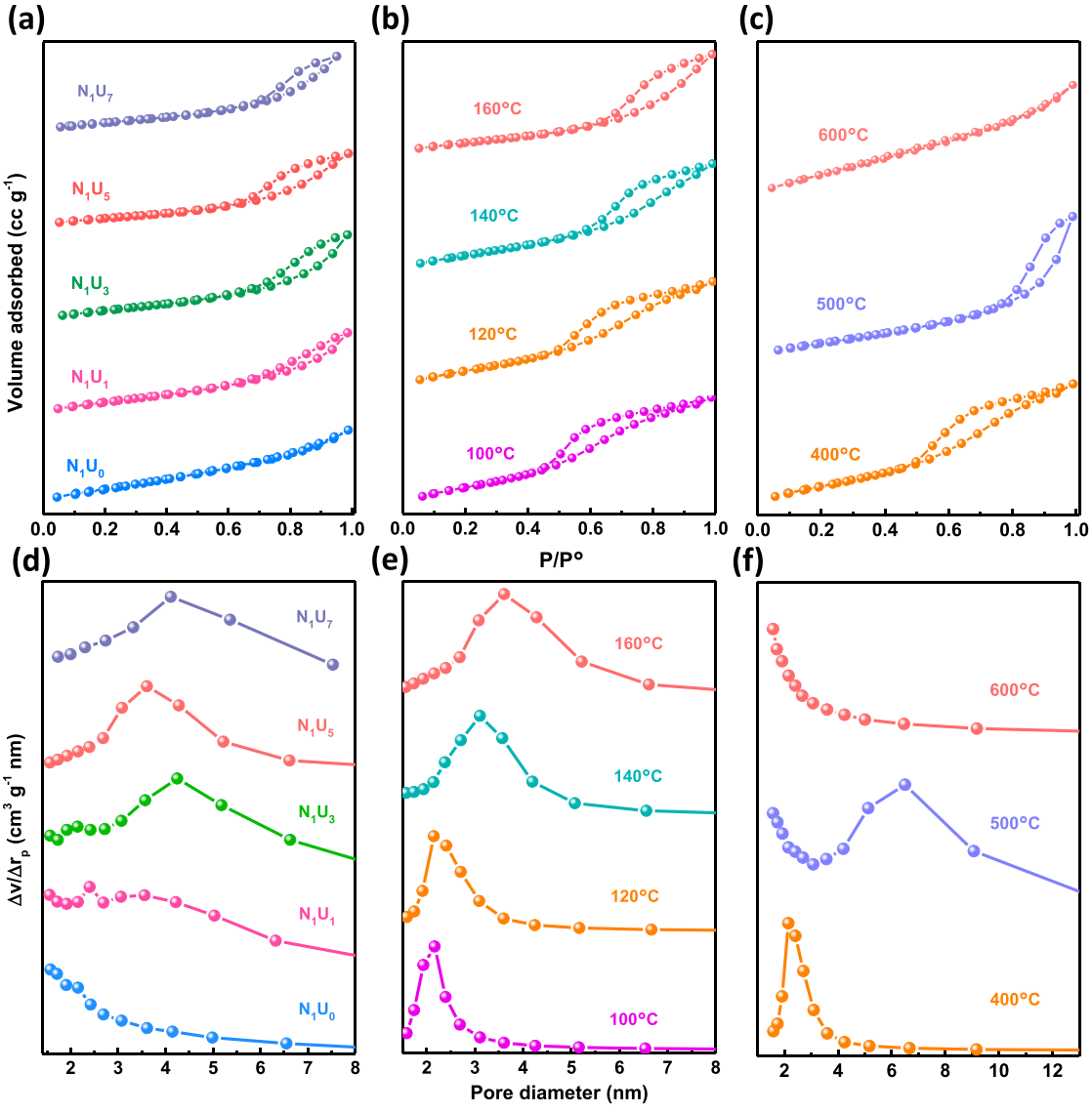

Fig. 5. N_2 sorption isotherms and Pore-size distribution curves of: (a,d) N_1U_y catalyst series, (b,e) N_1U_5 catalysts synthesized at various hydrothermal preparation temperatures, (c,f) N_1U_5 catalysts synthesized at various annealing temperatures.

Table 2
Surface texture of N_1U_y catalysts.

Catalyst	Specific surface area ($m^2\ g^{-1}$)		Total pore volume ($cc\ g^{-1}$) $*10^{-2}$	Average pore diameter (nm)	D_{BET} (nm)
	S_{BET}	S_t			
N_1U_0, 160 °C	20.9	20.9	9.0	1.6	73.6
N_1U_1, 160 °C	108.3	108.3	14.8	2.4	14.1
N_1U_3, 160 °C	120.5	120.5	25.9	4.3	12.7
N_1U_5, 160 °C	130.3	130.3	23.0	3.6	11.9
N_1U_7, 160 °C	117.3	117.3	18.9	4.1	13.1
N_1U_5, 100 °C	139.8	139.8	21.0	2.2	11.9
N_1U_5, 120 °C	154.5	154.5	24.1	2.2	10.0
N_1U_5, 140 °C	145.4	145.4	25.0	3.1	11.2
N_1U_5, 120 °C, 500 °C	85.2	85.2	14.9	6.5	18.2
N_1U_5, 120 °C, 600 °C	48.5	48.5	5.0	1.6	31.1

these trends: which show upward deviations for most catalysts, illustrating predominantly mesoporous structures. In contrast, pure $NiMoO_4$ (N_1U_0) and the N_1U_5 sample calcined at 600 °C display downward deviations, suggestive of microporosity and verify the outcomes of the pore size distribution method [75,79].

3.2. Acidity assessment

Assessing the total acidity and the distribution of acid-site strength is essential for understanding the factors governing catalytic activity and selectivity. Accordingly, IPA dehydration, chemisorption using basic probe molecules (PY, DMPY), and PY-TPD measurements were employed to investigate the overall acidity, nature, and strength of the surface acid sites. All catalytic tests were conducted at 225 °C. In all experiments, propene was the dominant reaction product, whereas acetone was detected only in trace amounts, confirming that the active surface sites are predominantly acidic. Fig. 6a illustrates the IPA dehydration performance of the N_1U_y catalysts synthesized hydrothermally at 160 °C and annealed at 400 °C. It indicates that increasing the urea ratios ($y = 0, 1, 3, 5$) leads to a marked increase in IPA conversion (44.8, 92.3, 93.5, and 95.2 %, respectively), accompanied by increasing propene selectivity (47, 91, 91.5, and 94 %). However, a further increase in urea conttent to $y = 7$ results in a decrease in both conversion (90 %) and selectivity (89 %), indicating that a Ni:urea ratio of 1:5 provides the highest acidity and optimal catalytic activity. Fig. 6b presents the impact of the hydrothermal preparation temperature on the IPA dehydration activity of N_1U_5 (subsequently annealed at 400 °C). The catalyst prepared at 120 °C shows the highest activity, achieving 99 % IPA conversion and 97 % propene selectivity. The effect of hydrothermal aging time for N_1U_5 synthesized hydrothermally at 120 °C and annealed at 400 °C is displayed in Fig. 6c. The results indicate that a hydrothermal treatment time of 12 h yields the highest IPA conversion and propene selectivity, which is consistent with the S_{BET} values (Table 2) [63]. Fig. 6d further displays the impact of annealing temperature of N_1U_5 synthesized hydrothermally at 120 °C for 12 h. It reveals that conversions decline when the annealing temperature treatment exceeds 400 °C. This decrease is ascribed to the reduction in surface area (S_{BET}) and the associated decrease in accessible acidic sites. Addition, the increased formation of β-$NiMoO_4$ at higher annealing temperatures, relative to α-phase, further reduces the number of active sites on the catalyst surface, as confirmed by the XRD results (Fig. 1c) [29,63,80].

Although IPA dehydration offers valuable insights into the overall acidity of the catalysts, it does not offer detailed information regarding

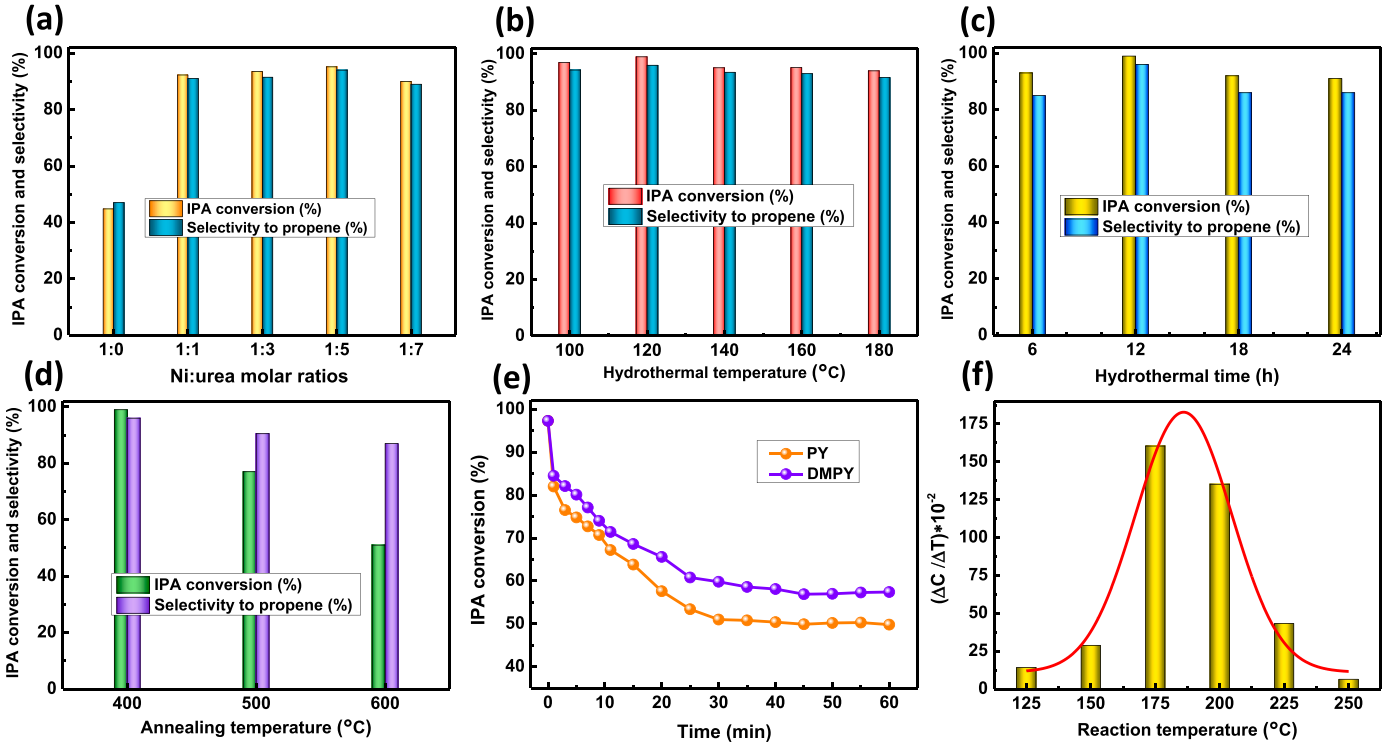

Fig. 6. IPA dehydration across (a) N_1U_y catalyst series, (b) N_1U_5 synthesized at various hydrothermal preparation temperatures, (c) N_1U_5 catalysts synthesized for various hydrothermal preparation times, and (d) N_1U_5 catalysts synthesized at various annealing temperatures, (e) IPA conversion as a function of PY and DMPY exposure times at 225 °C, over N_1U_5 catalyst; (f) Population of IPA conversion versus reaction temperature over PY-saturated N_1U_5 catalyst.

the type of acidic sites (Lewis or Brønsted) or their strength. Therefore, chemisorption of PY and DMPY was employed to distinguish the nature of the acidic sites. It is well established that PY can adsorb on both Lewis and Brønsted acid sites, whereas DMPY selectively interacts with Brønsted acid sites due to steric hindrance caused by its two methyl substituents, which limits its interaction with Lewis sites. Accordingly, the difference between the adsorption amounts of PY and DMPY can be used to determine the concentration of Lewis acid sites [40,78,81,82]. The effect of PY and DMPY adsorption on IPA conversion over N_1U_5, hydrothermally heated at 120 °C and annealed at 400 °C, is shown in Fig. 6e. As the exposure time to PY or DMPY increases, the IPA conversion gradually decreases and reaches a steady state after approximately 45 min, with conversion values of 49.9 % (PY) and 56.9 % (DMPY). The ~ 7 % difference is assigned to the presence of Lewis acidic sites, whereas the vast of surface acid sites are Brønsted in nature.

Therefore, the strength of the acidic sites was probed using two complementary approaches. In the first approach, temperature-dependent IPA conversion was measured over N_1U_5 pre-saturated with PY. The most efficient catalyst (N_1U_5) was exposed to PY vapor for seven days inside an evacuated desiccator to ensure adsorption on the acidic sites. Afterward, a known amount of the PY-treated catalyst was used for IPA dehydration at different reaction temperatures. The resulting conversion values were correlated with temperature, and the derivative of conversion with respect to temperature ($\Delta C/\Delta T$, where C represents conversion and T denotes reaction temperature) was plotted against temperature [41,83,84], as shown in Fig. 6f. As illustrated, most of the adsorbed PY molecules desorb between 175 and 200 °C, indicating that the catalyst surface predominantly contains moderately strength acid sites [63,80]. In the second approach, the strength of the acidic sites was further evaluated using thermogravimetric analysis of pyridine pre-adsorbed samples (PY-TPD) conducted in an air atmosphere [41,83,84], and the results are recorded in Table 3. In this experiment, about 20 mg of the pyridine-saturated catalyst was analyzed by thermogravimetry with a heating rate of 5 °C min^{-1} over a temperature range of 25–400 °C. The data listed in Table 3 are consistent with the IPA conversion data shown in Fig. 6a and b. Where the N_1U_5 catalyst synthesized hydrothermally at 120 °C exhibits higher acidity than the sample prepared at 160 °C. Moreover, analysis of the acidity distribution indicates that intermediate-strength acid sites predominate on the catalyst surface, whereas only minor amounts of weak and strong acidic sites are detected.

3.3. Catalytic dehydrogenation of MeOH to H_2 and FA production

3.3.1. Role of preparation and operating conditions in catalytic performance

In all catalytic runs carried out between 275 and 325 °C, dimethyl ether (DME) was detected as the primary byproduct, while H_2 and FA were formed simultaneously in equimolar amounts and exhibited identical selectivity profiles. Fig. 7a presents the evolution of % methanol conversion and selectivity toward H_2 and FA over the N_1U_y series which was synthesized at 160 °C for 12 h and annealed at 400 °C. At 325 °C, the % methanol conversion increases from 54.4 % to 77.8 % as the urea content (y-value) increases from 0 to 5, after which a slight decline is observed. H_2 and FA selectivity follows the same trend. These results identify N_1U_5 as the most active catalyst in the series, achieving 77.8 % conversion and 93 % selectivity toward H_2 and FA, consistent with the S_{BET} values (Table 2) and the acidity data (Table 3 and Fig. 6a). The enhanced activity relates to the abundance of sensitive terminal Mo═O groups and the existence of Mo^{6+} species acting as active acidic centers [85–87]. It is crucial to note that, the synergetic effect of α- and β-$NiMoO_4$ phases contributes to the catalytic performance in methanol dehydrogenation. Where the α-phase is considered to provide more accessible Ni^{2+} active sites, facilitating methanol adsorption and activation and promoting the formation of methoxy intermediates. In contrast, the β-phase contributes to structural stability and may enhance the redox interaction between Ni and Mo species. The interfacial regions between the two phases can generate additional active sites, defects, and improved charge-transfer pathways, thereby enhancing catalytic activity. This phase-boundary effect becomes more pronounced when both phases coexist. To clarify this point, we evaluated samples with different phase compositions. The sample predominantly composed of the α-phase with a very small amount of β-phase (N_1U_0), as shown in Fig. 1a, exhibited the lowest catalytic performance, which can be attributed to its lowest S_{BET} (Table 2) and weakest acidity (Table 3 and Fig. 6a). With increasing urea ratio from 0 to 5, the β-phase content increased, resulting in mixed α/β phases that showed improved catalytic performance, consistence with a synergistic phase interaction [88]. Given its superior performance, N_1U_5 was selected for detailed investigation of preparation and reaction parameters. Fig. 7b depicts the hydrothermal preparation temperature impact on N_1U_5 catalyst that was prepared for 12 h and heat-treated at 400 °C. The % of methanol conversion is improved by raising the hydrothermal preparation temperature from 100 to 120 °C; subsequent increases lead to a decrease in activity. At 325 °C, samples prepared at 100, 120, 140, 160, and 180 °C afford methanol conversions of 77.4, 80, 71.8, 77.8, and 59.8 %, respectively, with corresponding H_2 and FA selectivity's of 92.3, 96, 91.6, 93, and 91 %. Thus, 120 °C yields the optimal hydrothermal environment, in agreement with textural and acidity trends (Table 2, Table 3; Fig. 6b). Under these conditions, the N_1U_5 catalyst delivers 80 % conversion with 96 % selectivity toward H_2 and FA at 325 °C. The hydrothermal preparation time influence on the catalyst performance of N_1U_5 catalyst that synthesized at 120 °C and heat-treated at 400 °C, is shown in Fig. 7c. Among all samples, the catalyst prepared for 12 h exhibits the most outstanding conversion and selectivity, consistent with the acidity patterns shown in Fig. 6c. Previous experiments were conducted with a catalyst weight of 0.3 g; however, the effect of catalyst loading must be accounted for to avoid mass-transfer limitations. As depicted in Fig. 7d, the rising in the weight of catalyst from 0.1 to 0.5 g led to growth the % methanol conversion from 53.8 to 99 % with H_2 and FA selectivity from 89.2 to 97 %, beyond which no significant improvement occurs. The improved activity results from the increased availability of acidic sites [29,63,79]. Accordingly, 0.5 g is identified as the optimal catalyst loading. Under these conditions at 325 °C, the N_1U_5 catalyst yields 99 % methanol conversion with 97 % H_2 and FA selectivity. Fig. 7e shows the annealing temperature impact, in which rising the annealing treatment above 400 °C significantly reduces catalytic activity due to the loss of surface area (Table 2), and thus fewer accessible acidic active sites (Fig. 6d) [29,41,63,78]. Furthermore, as illustrated in XRD (Fig. 1c), as the annealing temperature rises, the β-phase grows, and this results in low conversion and selectivity. So, these results indicate that catalytic performance is governed by three important factors: phase composition, surface area and acidity. Therefore, the catalyst calcined at 400 °C provides the maximum performance, affording 99 % conversion, 97 %

Table 3
acidic site distributions across various N_1U_y catalyst series that annealed at 400 °C.

Catalyst	Total Acidity (Sites g^{-1}* 10^{20})	Strength/Sites g^1*10^{20}		
		RT-150 °C	150 -350 °C	>350 °C
N_1U_0, 160 °C	3.17	1.10	1.53	0.54
N_1U_1, 160 °C	14.8	5.31	6.48	3.02
N_1U_3, 160 °C	21.5	7.67	9.21	4.60
N_1U_5, 160 °C	21.9	7.91	9.52	4.47
N_1U_7, 160 °C	19.9	6.27	9.2	4.43
N_1U_5, 120 °C	54.0	19.0	25.1	9.90

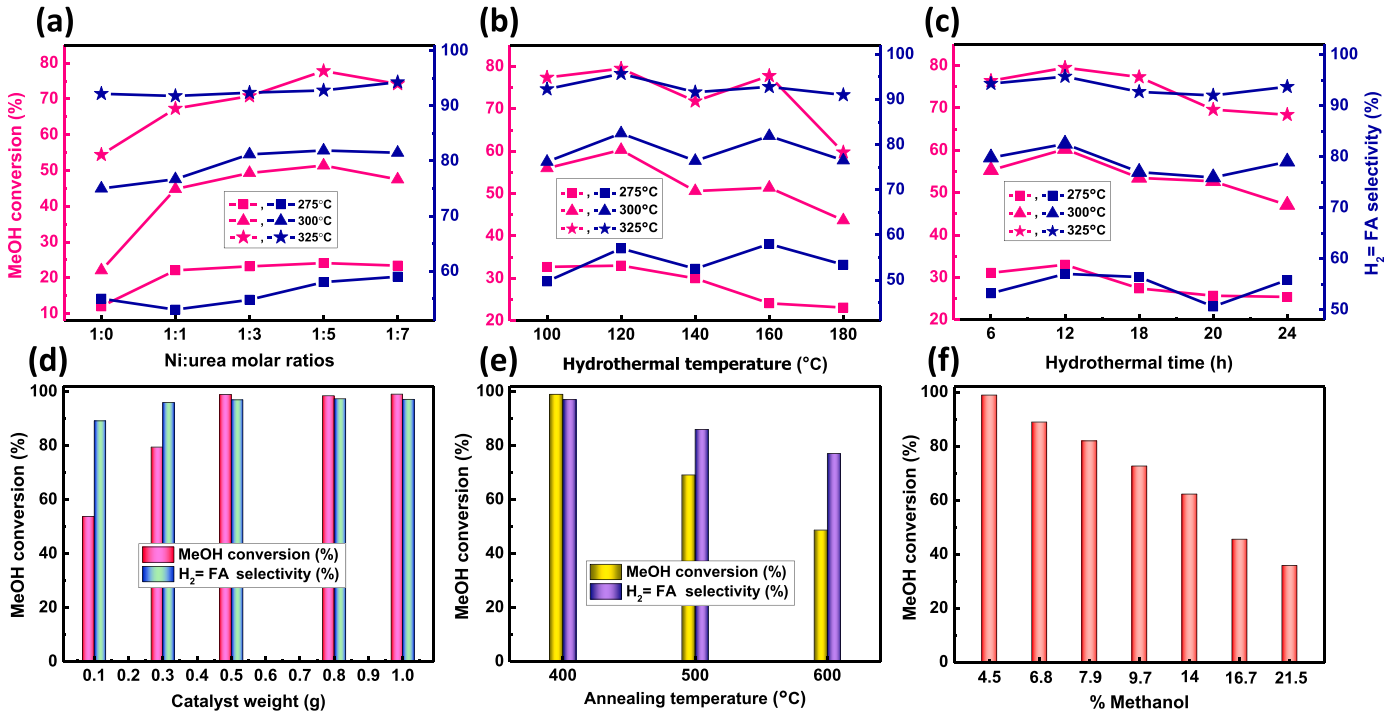

Fig. 7. Methanol conversion and H_2 = FA selectivity variations across (a) N_1U_y catalyst series, (b) N_1U_5 synthesized at various hydrothermal preparation temperatures, (c) N_1U_5 catalysts at various hydrothermal preparation times, and (d) the impact of catalyst weight over the optimized N_1U_5 catalyst, (e) N_1U_5 catalysts subjected to various annealing temperatures, (f) Influence of % methanol content on the dehydrogenation of methanol to FA over N_1U_5 catalyst.

H_2 and FA selectivity, and 3 % DME selectivity. The impact of the % methanol concentration in the feed stream over N_1U_5 (synthesized at 120 °C/12 h and heat-treated at 400 °C) is illustrated in Fig. 7f. The highest conversion (99 %) with H_2 and FA selectivity (97 %) are obtained at 4.5 % methanol. Increasing methanol concentration causes a gradual decrease in conversion, reaching 36 % at 21.5 % methanol while

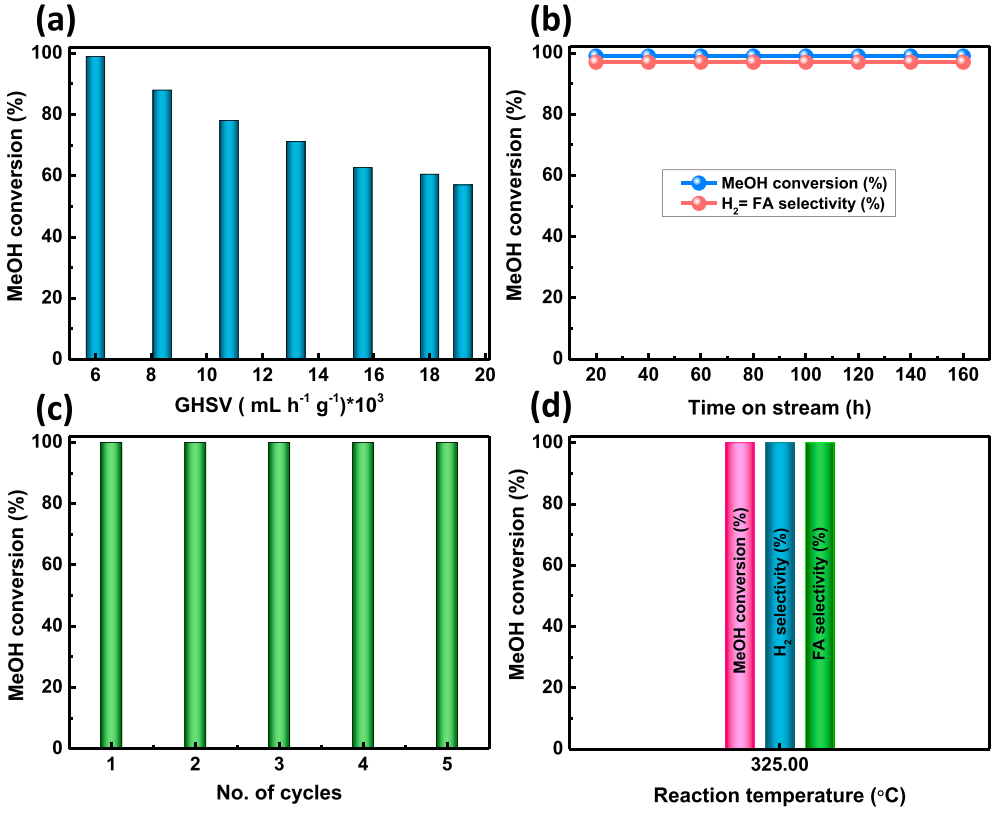

Fig. 8. (a) Influence of GHSV on the dehydrogenation of methanol to H_2 and FA over N_1U_5 catalyst, (b) catalyst stability, (c) recyclability under identical conditions, (d) optimized N_1U_5 catalyst obtained after systematic optimization of all experimental conditions, (All experiments conducted at 325 °C).

maintaining 97 % H_2 and FA selectivity. Notably, conversion remains as high as 89 % at 7 % methanol, which is industrially favorable. When compared with the previously reported $NiMoO_4$ ($N_1T_{1)}$ catalyst [63], the N_1U_5 catalyst exhibits higher conversion and selectivity, and its performance decreases less severely with increasing methanol content. This superior behavior likely originates from its higher specific surface area (Table 2), more moderate acidic site strength (Fig. 6f), and higher number of acidic sites (Table 3).

3.3.2. *Evaluation of stability and reusability of N_1U_5 catalyst*

The gas hourly space velocity (GHSV) influence over N_1U_5 (synthesized hydrothermally at 120 °C/12 h and heat-treated at 400 °C) is illustrated in Fig. 8a. The 99 % of methanol conversion was achieved by N_1U_5 catalyst at a GHSV of 6000 mL h^{-1} g^{-1}. The % conversion drops to 57 % when the GHSV is increased to 19,200 mL h^{-1} g^{-1} due to shorter contact time between reactant molecules and the catalyst surface [29,41,63,79,80]. The catalyst's long-term stability was examined at 325 °C for 168 h (Fig. 8b). N_1U_5 reaches 99 % conversion and 97 % H_2 and FA selectivity within 30 min of methanol introduction. After 5 h, the catalyst reaches complete (100 %) conversion with 100 % H_2 and FA selectivity and maintains this level for the remainder of the 168-h test, demonstrating excellent stability without deactivation. Recyclability was also examined and the outcomes are shown in Fig. 8c. After each cycle, the spent catalyst was projected to heat treatment at 400 °C for 3 h and reused for methanol dehydrogenation. As illustrated in Fig. 8c, the catalyst retains performance over five cycles, confirming robust regenerability. The spent catalyst was characterized by XRD and FT-IR, as presented in Fig. S4(a and b). The XRD pattern of the spent N_1U_5 catalyst shows some changes compared to the fresh sample, with slightly sharper diffraction peaks indicating a slight increase in crystallinity after reaction. The FT-IR spectra reveal two main differences. Firstly, a small decrease in the intensity of the band located at approximately 880 cm^{-1}, which is attributed to the tetrahedral coordination of Mo in the $NiMoO_4$ lattice and is characteristic of the β-phase. This band is commonly used to confirm the presence of β-$NiMoO_4$ [53,56,57]. The observed reduction in their intensity suggests a small decrease in the β-phase content, accompanied by a relative increase in the α-$NiMoO_4$ phase. This transformation is likely due to prolonged exposure of the catalyst to elevated temperatures (325 °C) during the reaction. The second change is the reduction in the intensity of the bands observed at 3427 and 1638 cm^{-1}, which are associated with surface hydroxyl groups. This decrease can be attributed to the partial removal of OH groups from the catalyst surface under reaction conditions [53,56,57,63,78]. Fig. 8d summarizes the performance of the N_1U_5 catalyst after comprehensive optimization of both catalyst synthesis and catalytic operating conditions. The catalyst exhibits complete conversion together with exclusive selectivity toward H_2 and FA, highlighting its promise and strong potential for large-scale industrial utilization.

To highlight the remarkable efficiency of our catalyst, the comparison presented in Table 4 shows that most previously reported catalysts for methanol non-oxidative dehydrogenation operate at relatively high temperatures to achieve moderate to high conversion and selectivity toward H_2 or FA. Despite these conditions, many catalysts still show limited selectivity or incomplete conversion. In contrast, the N_1U_5 catalyst developed in this work exhibits outstanding catalytic performance at a significantly lower temperature of 325 °C, achieving complete methanol conversion with 100 % selectivity toward H_2 and FA. These results clearly highlight the superior efficiency of the present catalyst compared with previously reported systems in terms of both activity and operating temperature.

Table 4
Contrasting the present catalyst's catalytic performance with that previously documented in the literature.

Catalyst	Reaction temperature (°C)	Conversion (%)	H_2 = FA selectivity (%)	References
ZnO/SiO_2	550	57	77	[36]
Cu/SiO_2	500	50	80	[38]
Ag–SiO_2–MgO	650	96	78	[32]
Ag–SiO_2–Al_2O_3 –ZnO	650	99	87	[34]
In_2O_3/Na_2CO_3	677	60	75	[33]
La–ZnO/SiO_2	600	34	73	[35]
$4Ga/SiO_2$	550	74	70	[37]
β-Ga_2O_3	500	65	70	[39]
5 wt% MoO_3/ HAP.	400	100	97	[40]
$CaMoO_4$	400	100	98	[41]
SO_4^{2-}-$Ce_2(MoO_4)_3$/ SiO_2	350	100	100	[42]
$Zr(MoO_4)_2$ with Zr:TEA ratio 1:1 (Z_1T_1)	325	99	95	[29]
$NiMoO_4$ with Ni: urea ratio 1:5 (N_1U_5)	325	100	100	Our work

3.4. *Reaction mechanism*

Based on the structural, surface, and catalytic characterization results, a mechanism for methanol dehydrogenation to H_2 with concurrent FA over $NiMoO_4$ is proposed (Scheme 2), establishing a direct structure-property-performance relationship. Initially, methanol adsorbs onto the catalyst surface via hydrogen bonding between its hydroxyl group (–OH) and the oxygen atom of Mo═O species. Subsequently, the Mo═O group abstracts a proton from methanol, leading to O–H bond cleavage and the formation of a surface methoxy intermediate (–OCH_3). This step is thermally activated at the reaction temperature of 325 °C and is accompanied by partial reduction of Mo^{6+} to Mo^{5+}, as evidenced by XPS analysis. The presence of electron-rich Mo^{5+} species enhances the nucleophilicity of the active sites, facilitating subsequent dehydrogenation steps [71]. The next step involves cleavage of the α-C–H bond of the methoxy intermediate, which is kinetically more demanding than O–H bond dissociation and is therefore considered the rate-determining step. This process is promoted by the synergistic interaction between Ni and Mo species. Nickel acts as a redox-active center (e.g., $Ni^{2+} \leftrightarrow Ni^{3+}$), facilitating electron transfer to Mo sites and thereby activating them for efficient C–H bond scission. This Ni–Mo cooperation plays a critical role in maintaining high catalytic activity and selectivity toward FA [89–92]. Following C–H bond cleavage, FA (HCHO) is formed and weakly adsorbed on the catalyst surface, allowing its rapid desorption. Meanwhile, hydrogen species generated during O–H and C–H activation undergo proton-coupled electron transfer (PCET) to form molecular H_2, completing the catalytic cycle and regenerating the active sites. Importantly, the proposed mechanism is consistent with the experimental findings, highlighting the critical role of catalyst structure in governing performance. The catalytic behavior is strongly influenced by the coexistence of α- and β-$NiMoO_4$ phases, as well as by surface acidity, and specific surface area (S_{BET}). The α-phase provides accessible Ni^{2+} active sites that promote methanol adsorption and activation, whereas the β-phase enhances structural stability and strengthens Ni–Mo redox interactions (Ni^{2+} and Mo^{6+}/Mo^{5+} species). In addition, the α/β interfacial regions generate defects and additional active sites, facilitating charge transfer and improving catalytic efficiency. The superior performance of the optimized N_1U_5 catalyst is attributed to its higher surface area and acidity, as confirmed by N_2 adsorption and acidity measurements (IPA and PY-TPD), which enhance methanol adsorption and intermediate stabilization. Furthermore, improved electron mobility across α/β interfaces lowers the activation barrier for the rate-determining step. Consequently, the outstanding catalytic performance (100 % conversion and selectivity) arises from the synergistic combination of optimal phase composition, high surface area, enhanced acidity, and strong interfacial interactions, all of which promote

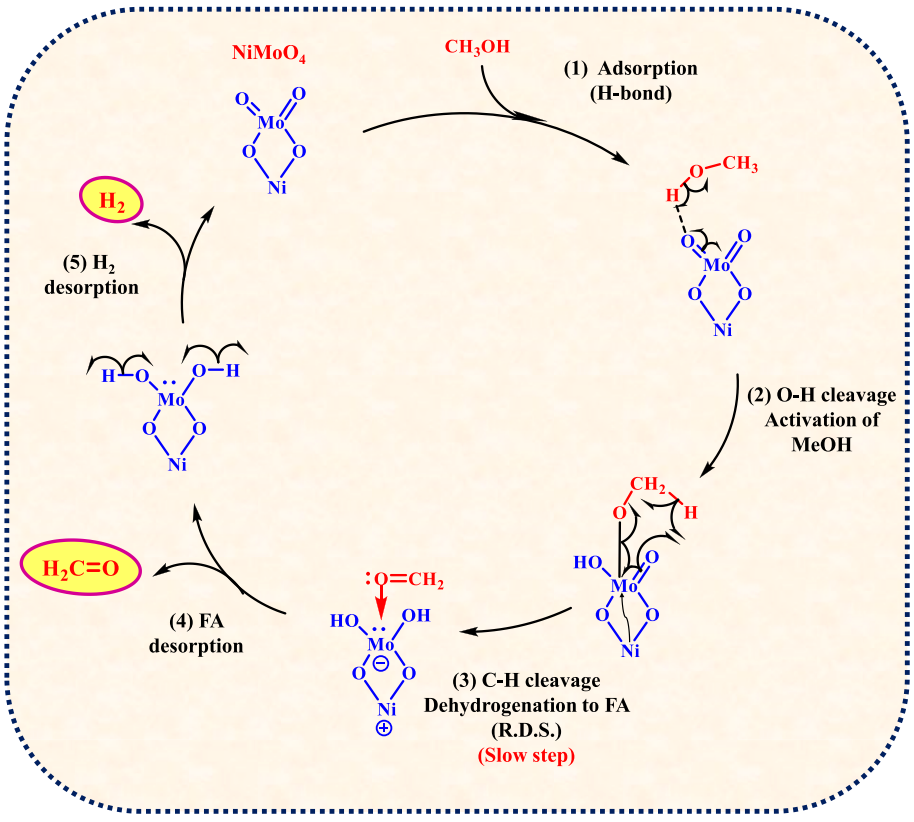

Scheme 2. The suggested mechanism for the catalytic dehydrogenation of MeOH to CH_2O over N_1U_5 catalyst.

efficient methanol activation, charge transfer, and product formation [89–92].

4. Conclusion

$NiMoO_4$ nanostructures were successfully synthesized through a hydrothermal route employing urea as a fuel and subsequently evaluated as catalysts for the non-oxidation dehydrogenation of methanol to H_2 and FA dual production. The most active catalyst was N_1U_5 that was synthesized hydrothermally at 120 °C for 12 h and heat-treated at 400 °C. It exhibited 100 % conversion and 100 % H_2 and FA selectivity at 325 °C, compared to other catalysts. The XRD patterns showed mixed phases of α- $NiMoO_4$ and β- $NiMoO_4$ in a monoclinic crystal system. The morphology of N_1U_5 is nanoflowers which are confirmed by SEM and TEM images. These morphologies provide great surface area (154.4 m^2g^{-1}) and porosity, which has mesoporous nature. The Brønsted acid sites with moderate strength were seen in our catalysts. Various parameters affecting catalytic activity were examined perfectly to provide the final catalyst (N_1U_5). The most active catalyst exhibited remarkable stability up to 168 h on stream. Finally, the dual production of H_2 and FA from methanol using advanced catalysts such as nanoflower like $NiMoO_4$ represents a strategic approach to addressing both industrial and environmental challenges. This process not only ensures the efficient utilization of methanol but also supports the goals of green chemistry, carbon neutrality, and energy sustainability.

CRediT authorship contribution statement

Aya Farouk Farghal: Writing – review & editing, Writing – original draft, Validation, Methodology, Investigation, Formal analysis, Data curation, Conceptualization. **Abd El-Aziz Ahmed Said:** Supervision, Resources. **Mohamed Nady Goda:** Supervision. **Shiao-Wei Kuo:** Writing – review & editing, Visualization, Resources. **Mohamed M.M. Abd El-Wahab:** Writing – review & editing, Supervision, Resources.

Declaration of competing interest

The authors declare that they have no known competing financial interests or personal relationships that could have appeared to influence the work reported in this paper.

Appendix A. Supplementary data

Supplementary data to this article can be found online at https://doi.org/10.1016/j.ijhydene.2026.155112.

References

[1] Segovia-Hernández JG, Hernández S, Cossío-Vargas E, Juarez-García M, Sánchez-Ramírez E. Green hydrogen production for sustainable development: a critical examination of barriers and strategic opportunities. RSC Sustain 2025;3:134–57. https://doi.org/10.1039/D4SU00630E.
[2] Alamiery A. Advancements in materials for hydrogen production: a review of cutting-edge technologies. ChemPhysMater 2024;3:64–73. https://doi.org/10.1016/J.CHPHMA.2023.09.002.
[3] Sakthivel V, Jin Yoo D. Enhanced solid-electrolyte interface efficiency for practically viable hydrogen-air fuel cell systems. J Energy Chem 2025;100:356–68. https://doi.org/10.1016/J.JECHEM.2024.08.046.
[4] Gan G, Hong G, Zhang W. Active hydrogen for electrochemical ammonia synthesis. Adv Funct Mater 2025;35:2401472. https://doi.org/10.1002/ADFM.202401472.
[5] AlZahrani AA, Zamfirescu C, El-Emam RS. Analysis of a solar-assisted crude oil refinery system with onsite green hydrogen generation: a case study. Arab J Sci Eng 2024;50:2557–71. https://doi.org/10.1007/S13369-024-09191-3.
[6] Romero-Piñeiro L, Villanueva Perales AL, Haro P. Low-emission hydrogen supply chain for oil refining: assessment of large-scale production via electrolysis and gasification. Int J Hydrogen Energy 2025;97:338–49. https://doi.org/10.1016/J.IJHYDENE.2024.11.448.
[7] Hossain Bhuiyan MM, Siddique Z. Hydrogen as an alternative fuel: a comprehensive review of challenges and opportunities in production, storage, and transportation. Int J Hydrogen Energy 2025;102:1026–44. https://doi.org/10.1016/J.IJHYDENE.2025.01.033.
[8] Sun H, Wang Z, Meng Q, White S. Advancements in hydrogen storage technologies: enhancing efficiency, safety, and economic viability for sustainable energy transition. Int J Hydrogen Energy 2025;105:10–22. https://doi.org/10.1016/J.IJHYDENE.2025.01.176.

[9] Ali MS, Hossain Khan MS, Tuhin RA, Kabir MA, Azad AK, Farrok O. Hydrogen energy storage and transportation challenges: a review of recent advances. Hydrog Energy Convers Manag 2024:255–87. https://doi.org/10.1016/B978-0-443-15329-7.00001-6.

[10] Elegbeleye I, Oguntona O, Elegbeleye F. Green hydrogen: pathway to net zero Green House gas emission and global climate change mitigation. Hydrog 2025;6:29. https://doi.org/10.3390/HYDROGEN6020029.

[11] Kamran M, Turzyński M. Exploring hydrogen energy systems: a comprehensive review of technologies, applications, prevailing trends, and associated challenges. J Energy Storage 2024;96:112601. https://doi.org/10.1016/J.EST.2024.112601.

[12] Karibe H, Sair S, Faik A, Ait Ousaleh H. Electrified steam methane reforming: a review of heating technologies, challenges, and prospects. Int J Hydrogen Energy 2025;133:200–13. https://doi.org/10.1016/J.IJHYDENE.2025.04.475.

[13] Mezaal NA, Kalyutik AA, Hashem HS, Rasool BHA, Ali QA. Low-carbon hydrogen production technologies: a review of steam methane reforming and methane pyrolysis. Int J Energy Convers 2024;12:174–83. https://doi.org/10.15866/IRECON.V12I5.24801.

[14] Boruah A, Phukan A, Singh S. Utilization of coal for hydrogen generation. Int J Coal Prep Util 2024;45:1412–33. https://doi.org/10.1080/19392699.2024.2387651.

[15] Chen F, Chen B, Ma Z, Mehana M. Economic assessment of clean hydrogen production from fossil fuels in the intermountain-west region, USA. Renew Sustain Energy Transit 2024;5:100077. https://doi.org/10.1016/J.RSET.2024.100077.

[16] Formaldehyde Market - Industry Structure Evaluation. Demand drivers analysis, regional growth analysis and identification, competitive positioning review & global market size forecast to 2032. https://www.maximizemarketresearch.com/market-report/global-formaldehyde-market/23567/.

[17] Dorieh A, Selakjani PP, Shahavi MH, Pizzi A, Movahed SG, Pour MF, Aghaei R. Recent developments in the performance of micro/nanoparticle-modified urea-formaldehyde resins used as wood-based composite binders: a review. Int J Adhes Adhes 2022;114:103106. https://doi.org/10.1016/J.IJADHADH.2022.103106.

[18] Hao X, Li Z, Xiao M, Han D, Huang S, Xi G, Wang S, Meng Y. A phosphonated phenol-formaldehyde-based high-temperature proton exchange membrane with intrinsic protonic conductors and proton transport channels. J Mater Chem A 2022;10:10916–25. https://doi.org/10.1039/D2TA00986B.

[19] Iftikhar A, Qaiser Z, Sarfraz W, Ejaz U, Aqeel M, Rizvi ZF, Khalid N. Understanding the leaching of plastic additives and subsequent risks to ecosystems. Water Emerg Contam Nanoplastics 2024;3:5. https://doi.org/10.20517/WECN.2023.58.

[20] Tahsin A Al, Saha T, Saha S, Saha S, Ahamed F. Development of a biodegradable and eco-friendly novel printing composite using biomaterials on textile substrate and assessing the characterization. Sci Rep 2025;15:1–10. https://doi.org/10.1038/S41598-025-99507-6.

[21] Tari SM, Athalye AR. Biodegradability and sustainability in textile finishing—current challenges and future perspectives. Sustain Finish Tech Text 2025:17–39. https://doi.org/10.1007/978-981-96-4860-3_2.

[22] Yang Z, Yuan B, Wu P, He J, Liu C, Jiang W. Bifunctional chitosan-modified urea-formaldehyde fertilizer for soil restoration and slow, sustained nitrogen release. Environ Res 2025;279:121902. https://doi.org/10.1016/j.envres.2025.121902.

[23] Zhang L. Introduction to formaldehyde. R Soc Chem 2018:1–19. https://doi.org/10.1039/9781788010269-00001.

[24] Andersson A, Holmberg J, Häggblad R. Process improvements in methanol oxidation to formaldehyde: application and catalyst development. Top Catal 2016;59:1589–99. https://doi.org/10.1007/s11244-016-0680-1.

[25] Mahdi HI, Ramlee NN, Santos DH da S, Giannakoudakis DA, de Oliveira LH, Selvasembian R, Azelee NIW, Bazargan A, Meili L. Formaldehyde production using methanol and heterogeneous solid catalysts: a comprehensive review. Mol Catal 2023;537:112944. https://doi.org/10.1016/j.mcat.2023.112944.

[26] Silva Olaya AR, Kühling F, Mahr C, Zandersons B, Rosenauer A, Weissmüller J, Wittstock G. Promoting effect of the residual silver on the electrocatalytic oxidation of methanol and its intermediates on nanoporous gold. ACS Catal 2022;12:4415–29. https://doi.org/10.1021/ACSCATAL.1C05160.

[27] Millar GJ, Collins M. Industrial production of formaldehyde using polycrystalline silver catalyst. Ind Eng Chem Res 2017;56:9247–65. https://doi.org/10.1021/ACS.IECR.7B02388.

[28] Malik MI, Abatzoglou N, Achouri IE. Methanol to formaldehyde: an overview of surface studies and performance of an iron molybdate catalyst. Catalysts 2021;11:893. https://doi.org/10.3390/CATAL11080893.

[29] Said AEAA, Abd El-Wahab MMM, Farghal AF, Goda MN. Potential application of zirconium molybdate as a novel catalyst for the selective dehydrogenation of methanol to anhydrous formaldehyde. Sci Rep 2025;15:15384. https://doi.org/10.1038/S41598-025-96328-5.

[30] Parris D, Spinthiropoulos K, Ragazou K, Giovou A, Tsanaktsidis C. Methanol, a plugin marine fuel for Green House Gas Reduction—A review. Energies 2024;17:605. https://doi.org/10.3390/EN17030605.

[31] Jeong YR, Jung H, Kang J, Han JW, Park ED. Continuous synthesis of methanol from methane and steam over copper-mordenite. ACS Catal 2021;11:1065–70. https://doi.org/10.1021/ACSCATAL.0C04592.

[32] Ren LP, Dai WL, Cao Y, Fan KN. Novel highly active Ag-SiO_2-MgO catalysts used for direct dehydrogenation of methanol to anhydrous formaldehyde. Catal Letters 2003;85:81–5. https://doi.org/10.1023/A:1022172808752.

[33] Meyer A, Renken A. Sodium compounds as catalysts for methanol dehydrogenation to water-free formaldehyde. Chem Eng Technol 1990;13:145–9. https://doi.org/10.1002/CEAT.270130120.

[34] Ren LP, Dai WL, Yang XL, Cao Y, Li H, Fan KN. Novel highly active Ag-SiO_2-Al_2O_3-ZnO catalyst for the production of anhydrous HCHO from direct dehydrogenation of CH_3OH. Appl Catal Gen 2004;273:83–8. https://doi.org/10.1016/j.apcata.2004.06.015.

[35] Mušič A, Batista J, Levec J. Gas-phase catalytic dehydrogenation of methanol to formaldehyde over ZnO/SiO_2 based catalysts, zeolites, and phosphates. Appl Catal Gen 1997;165:115–31. https://doi.org/10.1016/S0926-860X(97)00195-6.

[36] Sagou M, Deguchi T, Nakamura S. Dehydrogenation of methanol to formaldehyde by ZnO-SiO_2 and Zn_2SiO_4 catalysts. Stud Surf Sci Catal 1989;44:139–46. https://doi.org/10.1016/S0167-2991(09)61288-X.

[37] Merko M, Delsing S, Busser GW, Muhler M. Non-oxidative dehydrogenation of methanol to formaldehyde over supported GaO_x-based catalysts. J Catal 2023;427:115111. https://doi.org/10.1016/J.JCAT.2023.115111.

[38] Yamamoto T, Shimoda A, Okuhara T, Misono M. A promoting effect of phosphorus-addition to Cu/SiO_2 on selective synthesis of formaldehyde by dehydrogenation of methanol. Chem Lett 1988;17:273–6. https://doi.org/10.1246/cl.1988.273.

[39] Merko M, Busser GW, Muhler M. Non-oxidative dehydrogenation of methanol to formaldehyde over bulk β-Ga_2O_3. ChemCatChem 2022;14. https://doi.org/10.1002/cctc.202200258.

[40] Said AEAA, El-Wahab MMMA, Alian AM. Selective oxidation of methanol to formaldehyde over active molybdenum oxide supported on hydroxyapatite catalysts. Catal Letters 2016;146:82–90. https://doi.org/10.1007/S10562-015-1624-2.

[41] Said AEAA, Goda MN. Superior catalytic performance of $CaMoO_4$ catalyst in direct dehydrogenation of methanol into anhydrous formaldehyde. Chem Phys Lett 2018;703:44–51. https://doi.org/10.1016/j.cplett.2018.05.009.

[42] Aeaa Said, Goda MN. Synthesis, characterization and catalytic activity of Nanocrystalline $Ce_2(MoO_4)_3$/SiO_2 as a novel catalyst for the selective production of anhydrous formaldehyde from methanol. Catal Letters 2019;149:419–30. https://doi.org/10.1007/s10562-018-2621-z.

[43] Yuvaraja R, Sarathkumar S, Gowsalya V, Anitha Juliet SP, Veeralakshmi S, Kalaiselvam S, Gunasekar GH, Nehru S. Rational design of $NiMoO_4$/carbon nanocomposites for high-performance supercapacitors: an in situ carbon incorporation approach. Energy Adv 2025;4:94–105. https://doi.org/10.1039/D4YA00438H.

[44] Li E, Liu L, Han L, Guo C, Liu P, Liu X. Microwave-assisted one-step synthesis of NiMoO4 and $NiMoO_4$·xH_2O/carbon composites and their application in supercapacitors. J Energy Storage 2025;121:116605. https://doi.org/10.1016/J.EST.2025.116605.

[45] Chebrolu VT, Balakrishnan B, Aravindha Raja S, Kim HJ. A facile synthesis of a NiMoO4@metal-coated graphene-ink nanosheet structure towards the high energy density of a battery type-hybrid supercapacitor. Dalt Trans 2020;49:9762–72. https://doi.org/10.1039/D0DT00624F.

[46] Rammal MB, Omanovic S. Synthesis and characterization of NiO, MoO_3, and $NiMoO_4$ nanostructures through a green, facile method and their potential use as electrocatalysts for water splitting. Mater Chem Phys 2020;255:123570. https://doi.org/10.1016/J.MATCHEMPHYS.2020.123570.

[47] Oudghiri-Hassani H, Wadaani F Al. Preparation, characterization and catalytic activity of nickel molybdate ($NiMoO_4$) nanoparticles. Molecules 2018;23. https://doi.org/10.3390/molecules23020273.

[48] Aishwarya K, Maruthasalamoorthy S, Mani J, Anbalagan G, Nirmala R, Navaneethan M, Navamathavan R. Structural formation of multifunctional $NiMoO_4$ nanorods for thermoelectric applications. Phys Chem Chem Phys 2022;24:25620–9. https://doi.org/10.1039/d2cp04057c.

[49] Zhang Y, Chang CR, Jia XD, Cao Y, Yan J, Luo HW, Gao HL, Ru Y, Mei HX, Zhang AQ, Gao KZ, Wang LZ. Influence of metallic oxide on the morphology and enhanced supercapacitive performance of $NiMoO_4$ electrode material. Inorg Chem Commun 2020;112:107697. https://doi.org/10.1016/J.INOCHE.2019.107697.

[50] Fan X, Li J, Zhao Z, Wei Y, Liu J, Duan A, Jiang G. Synthesis of a new ordered mesoporous $NiMoO_4$ complex oxide and its efficient catalytic performance for oxidative dehydrogenation of propane. J Energy Chem 2014;23:171–8. https://doi.org/10.1016/S2095-4956(14)60132-7.

[51] Yao M, Hu Z, Liu Y, Liu P. A novel synthesis of size-controllable mesoporous NiMoO4 nanospheres for supercapacitor applications. Ionics 2016;22:701–9. https://doi.org/10.1007/S11581-015-1587-8.

[52] Feng X, Ning J, Wang D, Zhang J, Xia M, Wang Y, Hao Y. Heterostructure arrays of NiMoO4 nanoflakes on N-doping of graphene for high-performance asymmetric supercapacitors. J Alloys Compd 2020;816:152625. https://doi.org/10.1016/J.JALLCOM.2019.152625.

[53] De Moura AP, De Oliveira LH, Rosa ILV, Xavier CS, Lisboa-Filho PN, Li MS, La Porta FA, Varela JA. Structural, optical, and magnetic properties of $NiMoO_4$ nanorods prepared by microwave sintering. Sci World J 2015;2015. https://doi.org/10.1155/2015/315084.

[54] Yesuraj J, Padmaraj O, Suthanthiraraj SA. Synthesis, characterization, and improvement of supercapacitor properties of $NiMoO_4$ nanocrystals with polyaniline. J Inorg Organomet Polym Mater 2020;30:310–21. https://doi.org/10.1007/S10904-019-01189-X.

[55] Simonenko TL, Bocharova VA, Simonenko NP, Simonenko EP, Sevastyanov VG, Kuznetsov NT. Formation of $NiMoO_4$ anisotropic nanostructures under hydrothermal conditions. Russ J Inorg Chem 2021;66:1779–84. https://doi.org/10.1134/S0036023621120160.

[56] Rammal MB, Omanovic S. Part I: $NiMoO_4$ nanostructures synthesized by the solution combustion method: a parametric study on the influence of synthesis parameters on the materials' physicochemical, structural, and morphological properties. Molecules 2022;27:776. https://doi.org/10.3390/molecules27030776.

[57] Shameem A, Devendran P, Siva V, Packiaraj R, Nallamuthu N, Asath Bahadur S. Electrochemical performance and optimization of α-$NiMoO_4$ by different facile

synthetic approach for supercapacitor application. J Mater Sci Mater Electron 2019;30:3305–15. https://doi.org/10.1007/s10854-018-00603-3.
[58] Yi TF, Qiu LY, Mei J, Qi SY, Cui P, Luo S, Zhu YR, Xie Y, He YB. Porous spherical NiO@$NiMoO_4$@PPy nanoarchitectures as advanced electrochemical pseudocapacitor materials. Sci Bull 2020;65:546–56. https://doi.org/10.1016/J.SCIB.2020.01.011.
[59] Murugan E, Govindaraju S, Santhoshkumar S. Hydrothermal synthesis, characterization and electrochemical behavior of $NiMoO_4$ nanoflower and $NiMoO_4$/rGO nanocomposite for high-performance supercapacitors. Electrochim Acta 2021;392:138973. https://doi.org/10.1016/J.ELECTACTA.2021.138973.
[60] Zhang M, Liu W, Han R, Xu J, Sun Z, Liu J, Wu Y. Facile construction of 3D packing porous flower-like $NiCo_2O_4$@$NiMoO_4$/rGO hybrids as high-performance supercapacitors with large areal capacitance. Energy Technol 2019;7:1800940. https://doi.org/10.1002/ENTE.201800940.
[61] Liao J, Wu Y, Shao Y, Feng Y, Zhang X, Zhang W, Li J, Wu M, Dong H, Liu Q, Li H. Ammonia borane methanolysis for hydrogen evolution on Cu3Mo2O9/NiMoO4 hollow microspheres. Chem Eng J 2022;449:137755. https://doi.org/10.1016/J.CEJ.2022.137755.
[62] Zhang L, Zhang M, Liu L, Wang Y, Zheng J, Xu J. Carbon-supported Ni and MoO_2 nanoparticles with Fe_3O_4 cores as a protein adsorbent. New J Chem 2020;44:15396–402. https://doi.org/10.1039/D0NJ02916E.
[63] Farghal AF, Said AE-AA, El-Wahab MMMA, Goda MN. Synthesis of a novel highly active $NiMoO_4$ nanocatalyst for the sustainable production of anhydrous formaldehyde from the non-oxidative dehydrogenation of methanol at relatively low temperature. Catal Lett 2024;155:1–17. https://doi.org/10.1007/S10562-024-04865-X.
[64] Zhang Y, Chang C-r, Jia X-d, Huo Q-y, Gao H-l, Yan J, Zhang A-q, Ru Y, Mei H-x, Gao K-z, Wang L-z. Morphology-dependent $NiMoO_4$/carbon composites for high performance supercapacitors. Inorg Chem Commun 2020;111:107631. https://doi.org/10.1016/J.INOCHE.2019.107631.
[65] Lv X, Min X, Lin X, Ni Y. Battery-type $NiMoO_4$@$NiMoS_4$ composite electrodes for high-performance supercapacitors. Chem Pap 2023;77:6655–67. https://doi.org/10.1007/S11696-023-02966-2.
[66] Muthu D, Vargheese S, Haldorai Y, Rajendra Kumar RT. $NiMoO_4$/reduced graphene oxide composite as an electrode material for hybrid supercapacitor. Mater Sci Semicond Process 2021;135:106078. https://doi.org/10.1016/J.MSSP.2021.106078.
[67] Caglar B, Hassan Y El, Basak O, Hepbasli A. Electrooxidation of glycerol on monometallic and bimetallic catalysts-containing porous carbon cloth electrodes in an alkaline medium. J Electrochem Soc 2021;168:084506. https://doi.org/10.1149/1945-7111/ac1a57.
[68] Sajjad S, Wang C, Wang X, Ali T, Qian T, Yan C. In situ evolved NiMo/$NiMoO_4$ nanorods as a bifunctional catalyst for overall water splitting. Nanotechnology 2020;31:495404. https://doi.org/10.1088/1361-6528/abb393.
[69] Biesinger MC, Payne BP, Grosvenor AP, Lau LWM, Gerson AR, Smart RSC. Resolving surface chemical states in XPS analysis of first row transition metals, oxides and hydroxides: cr, Mn, Fe, Co and Ni. Appl Surf Sci 2011;257:2717–30. https://doi.org/10.1016/j.apsusc.2010.10.051.
[70] Al-Salihy A, Zhu Q, Hu J, Liang C, Radwan AB, Salah A, Xu P. Synergistic effect of $NiMoO_4$ nanorods with polyaniline for efficient electrochemical water splitting. ACS Appl Mater Interfaces 2025;17:28199–210. https://doi.org/10.1021/ACSAMI.5C02693.
[71] Liu B, Wen H, Da B, Liang X, Li K, Xu Z, Zhang X, Zhang Y, Wang Y, Li H, Yan K. Effective electrocatalytic xylose oxidation coupling hydrogen production on hierarchical microcolumn $NiMoO_4$ array. Appl Catal B Environ Energy 2025;375:125443. https://doi.org/10.1016/J.APCATB.2025.125443.
[72] Patil SA, Jagdale PB, Iqbal A, Reza S, Jinagi M, Rajput P, Sfeir A, Royer S, Thapa R, Samal AK, Saxena M. Structural engineering of bimetallic $NiMoO_4$ for high-performance supercapacitors and efficient oxygen evolution reaction catalysts. J Mater Chem A 2025. https://doi.org/10.1039/D5TA02450A.
[73] Wang J, Li L, Meng L, Wang L, Liu Y, Li W, Sun W, Li G. Morphology engineering of nickel molybdate hydrate nanoarray for electrocatalytic overall water splitting: from nanorod to nanosheet. RSC Adv 2018;8:35131–8. https://doi.org/10.1039/C8RA07323F.
[74] Brunauer S, Deming LS, Deming WE, Teller E. On a Theory of the van der Waals Adsorption of Gases. J Am Chem Soc 1940;62:1723–32. https://doi.org/10.1021/JA01864A025.
[75] Leofanti G, Padovan M, Tozzola G, Venturelli B. Surface area and pore texture of catalysts. Catal Today 1998;41:207–19. https://doi.org/10.1016/S0920-5861(98)00050-9.
[76] Goda MN, El-Aal MA, Magdy E, Said AE-AA. The catalytic performance of $Fe_xMn_{1-x}WO_4$ as novel wolframite-type nanocatalysts for the selective dehydration of methanol into dimethyl ether. Mol Catal 2023;547:113350. https://doi.org/10.1016/j.mcat.2023.113350.
[77] Said AEAA, Abd El-Wahab MMM, Soliman SA, Goda MN. Synthesis and characterization of mesoporous Fe–Co mixed oxide nanocatalysts for low temperature CO oxidation. Process Saf Environ Prot 2016;102:370–84. https://doi.org/10.1016/J.PSEP.2016.04.015.
[78] Said AEAA, Goda MN, Shaban AA. The catalytic performance of ultrasonically prepared AlPO4 nanocatalysts for the selective production of Dimethyl Ether from methanol. Catal Letters 2022;152:821–37. https://doi.org/10.1007/s10562-021-03664-y.
[79] Said AEAA, Shaban AA, Goda MN. Zirconia incorporated aluminum phosphate molecular sieves as efficient microporous nano catalysts for the selective dehydration of methanol into Dimethyl Ether. Catal Lett 2023;1:1–18. https://doi.org/10.1007/S10562-023-04370-7.
[80] Goda MN, Farghal AF, El-Wahab MMMA, Said AEAA. Synthesis, characterization and catalytic activity of a novel zirconium molybdate nanocatalyst for methanol dehydrogenation at comparative low temperature. J Mol Struct 2025;1346:143213. https://doi.org/10.1016/J.MOLSTRUC.2025.143213.
[81] Said AEAA, Abd El-Wahab MMM, Alian AM. Catalytic performance of Brønsted acid sites during esterification of acetic acid with ethyl alcohol over phosphotungestic acid supported on silica. J Chem Technol Biotechnol 2007;82:513–23. https://doi.org/10.1002/JCTB.1704.
[82] Said AEAA, Abd El-Wahab MMM. Surface properties and catalytic behavior of MoO_3/SiO_2 in esterification of acetic acid with ethanol. J Chem Technol Biotechnol 2006;81:329–35. https://doi.org/10.1002/JCTB.1399.
[83] El-Aal MA, Said AEAA, Abdallah MH, Goda MN. Modified natural kaolin clay as an active, selective, and stable catalyst for methanol dehydration to dimethyl ether. Sci Reports 2022;12:1–13. https://doi.org/10.1038/s41598-022-13349-0.
[84] Goda MN, Said AEAA, Abdelhamid HN. Zirconium oxide sulfate-carbon ($ZrOSO_4$@C) derived from carbonized UiO-66 for selective production of Dimethyl Ether. Catal Letters 2020;12:646–53. https://doi.org/10.1021/acsami.9b17520.
[85] Kuang W, Fan Y, Chen K, Chen Y. Partial oxidation of toluene over ultrafine mixed Mo-Based oxide particles. J Catal 1999;186:310–7. https://doi.org/10.1006/JCAT.1999.2559.
[86] Saraya MEI, Rokbaa HHA. Preparation of vaterite calcium carbonate in the form of spherical nano-size particles with the aid of polycarboxylate superplasticizer as a capping agent. Am J Nanomater 2016;4:44–51. https://doi.org/10.12691/ajn-4-2-3.
[87] Kubo J, Ueda W. Catalytic behavior of $AMoO_x$ (A = Ba, Sr) in oxidation of 2-propanol. Mater Res Bull 2009;44:906–12. https://doi.org/10.1016/J.MATERRESBULL.2008.08.013.
[88] Zhang Y, Guo H, Li X, Ren W, Song R. The synergetic effect of the mixed phase of $NiMoO_4$ with a 1D–2D–3D hierarchical structure for a highly efficient and stable urea oxidation reaction. Mater Chem Front 2022;6:1477–86. https://doi.org/10.1039/d2qm00100d.
[89] Madeira LM, Portela MF, Mazzocchia C. Nickel molybdate catalysts and their use in the selective oxidation of hydrocarbons. Catal Rev 2004;46:53–110. https://doi.org/10.1081/CR-120030053.
[90] Wang S, Zhu J, Wu X, Feng L. Microwave-assisted hydrothermal synthesis of $NiMoO_4$ nanorods for high-performance urea electrooxidation. Chinese Chem Lett 2022;33:1105–9. https://doi.org/10.1016/J.CCLET.2021.08.042.
[91] Ray SK, Dhakal D, Regmi C, Yamaguchui T, Lee SW. Inactivation of Staphylococcus aureus in visible light by morphology tuned α-$NiMoO_4$. J Photochem Photobiol Chem 2018;350:59–68. https://doi.org/10.1016/J.JPHOTOCHEM.2017.09.042.
[92] Sudarsanam P, Gupta NK, Mallesham B, Singh N, Kalbande PN, Reddy BM, Sels BF. Supported MoO_x and WO_x solid acids for biomass valorization: interplay of coordination chemistry, acidity, and catalysis. ACS Catal 2021;11:13603–48. https://doi.org/10.1021/ACSCATAL.1C03326.